Research Square

Preprints are preliminary reports that have not undergone peer review.
They should not be considered conclusive, used to inform clinical practice,
or referenced by the media as validated information.

Correlation between bubble dynamics and arc stability during underwater wet welding initiation revealed by synchronized high-speed imaging and electrical signal analysis

Ziyang Lu
Yanshan University
Hao Chen
chenhao@ysu.edu.cn
Yanshan University https://orcid.org/0000-0003-3461-1638
Zhengxian Liu
Beijing System Design Institute of Electro-mechanic Engineering
Rui Xi
Yanshan University
Lerong Zhao
Yanshan University
Chenyi Yan
Yanshan University
Zeshi Jin
Zhejiang Industry Polytechnic College
Feng Yu
Zhejiang Industry Polytechnic College

Research Article

Keywords: Underwater wet welding, Bubble dynamic behavior, Arc stability, High-speed imaging, Electric signal acquisition

Posted Date: November 10th, 2026

DOI: https://doi.org/10.21203/rs.3.rs-11383620/v1

License: This work is licensed under a Creative Commons Attribution 4.0 International License.
Read Full License

Correlation between bubble dynamics and arc stability during underwater wet welding initiation revealed by synchronized high-speed imaging and electrical signal analysis

Ziyang Lu[a], Hao Chen[a*], Zhengxian Liu[b], Rui Xi[a], Lerong Zhao[a], Chenyi Yan[a], Zeshi Jin[c], Feng Yu[c]

a School of Mechanical Engineering, Yanshan University, Qinhuangdao 066004, China

b Beijing System Design Institute of Electro-mechanic Engineering, Beijing, 100854, China

c Zhejiang Industry Polytechnic College, Shaoxing 312000, China

Address: No. 438 West Hebei Avenue, Qinhuangdao, Hebei 066004, China

E-mail: chenhao@ysu.edu.cn

Abstract

Dynamic behavior of arc bubbles strongly affects arc stability and weld quality in underwater wet welding. Most existing research concentrates on the overall welding process, whereas the initial arc bubble formation at arc ignition remains understudied. In this work, synchronized high-speed imaging and electrical signal acquisition were used to investigate how contact tip-to-work distance (CTWD), wire feed speed and welding voltage affect bubble features and arc stability during arc ignition. Box-Behnken response surface methodology was applied to quantify the effects of the three parameters on maximum bubble radius and bubble lifetime. Arc bubbles show distinct morphologies in growth and collapse stages: horizontally elongated ellipsoids while growing and vertically stretched approximate cones during collapse. Significant interaction exists among CTWD (16 mm), wire feed speed (5 m/min) and welding voltage (31 V), jointly optimizing bubble radius and duration. At the arc initiation stage, reduced maximum bubble radius lowers current variation and unstable arc occurrence. Smaller initial bubbles also mitigate fluctuations of instantaneous heat input, reduce weld pores and macroscopic defects, modify microstructure and improve weld appearance. This work offers new understanding of arc bubble evolution and arc stability during arc ignition of underwater wet welding.

Keywords: Underwater wet welding; Bubble dynamic behavior; Arc stability; High-speed imaging; Electric signal acquisition

1.Introduction

Over the past few decades, the marine economy has become a new driver of global economic growth. Against this backdrop, underwater welding technology plays an indispensable role across various marine engineering applications, including the construction of offshore bridges and oil drilling platforms, the emergency repair of submarine oil pipelines and naval vessels, as well as shipwreck salvage operations. [1]. To meet the demand for high-quality maintenance of marine structures, underwater welding technology is undertaking increasingly important missions [2,3]. Depending on whether the welding zone is in direct contact with water, underwater welding can be classified into dry welding, local dry welding, and wet welding. As a method that isolates the welding zone from the water environment, dry underwater welding offers the most stable arc combustion, thereby enabling high-quality welds [4]. Relative to both dry welding and local dry welding, underwater wet welding (UWW) is distinguished by its lower cost and superior ease of operation. [5,6]. Nevertheless, the stability of the arc and the quality of welded joints are severely constrained by the negative effects of the surrounding water and generated bubbles. As a result, understanding how the wet welding process interacts with the underwater environment has become an urgent research priority and is regarded as one of the most significant challenges in underwater wet [7].

UWW is characterized by direct exposure to the surrounding water environment. Under such conditions, arc bubbles are produced from two sources: water ionization and decomposition, plus boiling triggered by the heat of the arc. The presence of these bubbles readily interferes with multiple aspects of the welding process, including arc behavior, droplet transfer, weld geometry, and final joint performance. At the moment of contact between the wire and the base metal surface, a large amount of heat is released, causing the surrounding water to vaporize and ionize, thereby generating welding gases that expand outward and rise to form welding bubbles [8]. When the bubble neck undergoes contraction and subsequent detachment, a narrower gas flow path accompanied by elevated flow velocity emerges. This combination renders the droplet more prone to the repulsive effect generated by the gas flow.Serious degradation of welding quality results from multiple issues, namely arc bubble collapse, insufficient arc stability, rapid cooling of the weld, and a strong tendency toward hydrogen-induced cracking [9]. Liao et al. employed high-energy synchrotron X-ray diffraction to characterize microstructural gradients and residual stress distributions in underwater welded joints, demonstrating the capability of advanced X-ray characterization to assess welding-induced changes in material integrity [10].

To address these challenges, numerous researchers have recently investigated the fundamental physical characteristics of the UWW process, including the growth behavior of arc bubbles, droplet transfer modes, and molten pool flow and heat transfer characteristics. Based on these investigations, various novel UWW methods assisted by

external energy fields have been developed. Yang et al. captured the arc shape during UWW using a high-speed camera and revealed the mechanisms of arc column constriction and arc length shortening from the perspectives of water environment cooling, gas composition within the arc bubble, and gas flow disturbance [11]. Feng et al. identified bubble evolution patterns and corresponding welding arc information under four typical conditions during UWW: low wire feed speed, medium wire feed speed, high wire feed speed, and high arc voltage. They found that under the third condition, bubbles floated smoothly without arc extinction, indicating good arc stability. Moreover, the study found that better protection provided by the bubbles could be achieved through a lower floating frequency and a larger maximum bubble diameter without extinguishing the arc, thereby enabling a more stable welding process [12]. Chen et al. employed X-ray imaging to observe the effect of arc bubble behavior on droplet transfer in underwater wet flux-cored arc welding (FCAW). Their research revealed a much higher arc bubble expansion rate at the initial stage relative to the later growth stage [13]. Greater bubble resistance therefore characterizes the early phase. When bubble expansion occurs too rapidly, the droplet deflection angle increases. This enlarged angle is identified as a key contributor to droplet repulsive spatter and unstable droplet transfer. Zhang et al. employed high-speed in situ X-ray imaging and electrical signal analysis to investigate the interactions among bubble evolution, molten slag dynamics, and droplet transfer during underwater wet welding. Their results demonstrated that stable molten-slag coverage mitigated bubble-induced disturbances and reduced electrical signal fluctuations, highlighting the relationship between observable process dynamics and welding stability [14]. Chen et al. applied lateral ultrasonic waves during welding and found that as the ultrasonic incidence angle increased, a change in bubble shape-from a sphere to a concave disc-conferred multiple advantages: suppression of free upward arc bubble floatation, reduction of the repulsive force acting upon the droplet, and stabilization of the welding electrical signals. [15]. Chen et al. investigated how the geometry of the ultrasonic radiator end face influences performance. They reported that a planar end face achieves the highest sound pressure, which in turn decreases the bubble separation size and separation angle while increasing the separation frequency. This design modification brought about an alteration in microstructure morphology. Consequently, the joint showed superior hardness, tensile strength, and impact toughness compared to unmodified conditions. [16]. Wang et al. applied a mechanically constrained underwater wet welding (MC-UWW) approach. They observed that this method restricted the free movement of bubbles, suppressed bubble-induced disturbances, and led to more consistent bubble morphology and dynamics. This allowed the bubble behavior to be better decoupled from that of the arc, ultimately resulting in a stable welding process. [17]. Wang et al. applied in-situ visual sensing to investigate arc bubble dynamic behavior during welding. By comparing different welding conditions, they characterized the evolution of these bubbles. Additionally, their research explored how deliberately

controlled arc bubbles influence welding process stability and the microstructural changes occurring in welded joints. The study found that mechanical constraint in UWW effectively resisted arc bubble detachment, allowing larger arc bubbles to adhere to the molten pool surface, thereby providing better protection to the welding zone. In contrast to the martensitic structure observed in the weld microstructure of conventional UWW, no martensitic microstructure was observed in MC-UWW [18]. Yang et al. demonstrated that spatial position influences both arc bubble behavior and arc stability in underwater wet welding. For vertical welding, arc bubbles readily escape the welding zone, impairing their arc-shielding capability. In contrast, during overhead welding, the workpiece obstructs bubble upward floatation, causing bubbles to linger and adhere to the workpiece surface. This sustained bubble presence preserves arc protection and leads to improved process stability [19].

Despite these advances in the visualization and characterization of underwater welding processes, the quantitative relationship between transient bubble dynamics and simultaneously acquired electrical signals during arc initiation remains insufficiently understood. In particular, how measurable bubble characteristics correlate with electrical signal fluctuations and arc instability has not been systematically established. In practical production, the stability of the arc initiation stage significantly affects the stability of the overall welding process and weld formation.

Arc bubbles exert both protective and perturbing effects on the welding arc column. Therefore, this study focuses on the dynamic evolution of arc bubbles during the arc initiation stage of underwater wet welding and its influence on arc burning stability. A synchronized high-speed imaging and electrical signal acquisition system was employed to capture bubble morphology and electrical signals during arc initiation under varying contact tip-to-work distances (CTWD), wire feed speeds, and welding voltages. The effects of multiple factors on bubble behavior and arc stability during the arc initiation stage were analyzed. A Box–Behnken design (BBD)-based response surface methodology was then adopted. The maximum bubble radius and bubble duration served as response variables for this analysis. Through this approach, we investigated the influence of different factors on arc initiation bubbles and derived predictions for the optimal bubble radius and bubble duration. In the final step, a relationship linking the maximum bubble radius, the coefficient of variation, and arc stability was developed. The weld microstructure was analyzed, and mechanical property tests were conducted. By presenting these findings, this study contributes a new reference point for advancing the understanding of bubble dynamics and arc stability during the arc initiation stage.

2. Experimental procedure

This research investigates bubble behavior and arc stability during the arc initiation phase of underwater wet

flux-cored arc welding (FCAW). The base metal used in the welding experiments was EH40 marine steel, a material of considerable practical value due to its widespread application in marine engineering. It measured 140 mm in length, 42 mm in width, and 8 mm in height. The welding consumable consisted of an ER2209 duplex stainless steel flux-cored wire with a 1.6 mm diameter. The chemical composition of the base metal, along with that of the welding wire, is summarized in Table 1.

Table 1 Chemical makeup of the base and filler materials (wt.%)

Material	C	Si	Mn	Cr	Ni	Mo	N	Fe
E40	0.17	0.45	1.36	0.02	0.05	-	-	Bal
ER2209	0.02	0.50	1.6	22.0	8.5	3.1	0.17	Bal

The underwater wet welding experimental platform used in this study, along with its synchronized high-speed imaging and electrical signal acquisition system, is illustrated in Fig. 1. A xenon lamp (CHF-XM500, Beijing Perfect Light Technology Co., Ltd.) was employed as the background light source, and a 900 nm wavelength laser was used for auxiliary illumination to enhance image clarity. To further improve imaging quality, the optical path of the recording system was optimized by adding a filter with a center wavelength matching that of the auxiliary laser in front of the lens, which effectively suppressed the interference from welding arc light and other stray light sources. During the welding process, a high-speed camera (Acuteye V4.0, Hunan Ketianjian Optoelectronics Co., Ltd.) was used to clearly capture the dynamic welding process, with particular attention paid to the evolution of the arc morphology and bubble behavior during the arc initiation stage.

A xenon lamp delivered a parallel 50 mm diameter illumination beam with an emission spectrum spanning 200-1000 nm. The imaging system recorded at 2000 fps with 1200 × 860 pixel resolution. By employing this optimized optical setup, we explored how arc bubbles behave dynamically during the arc initiation stage under diverse operational conditions-specifically, different contact tip-to-work distances, wire feed speeds, and welding voltages.

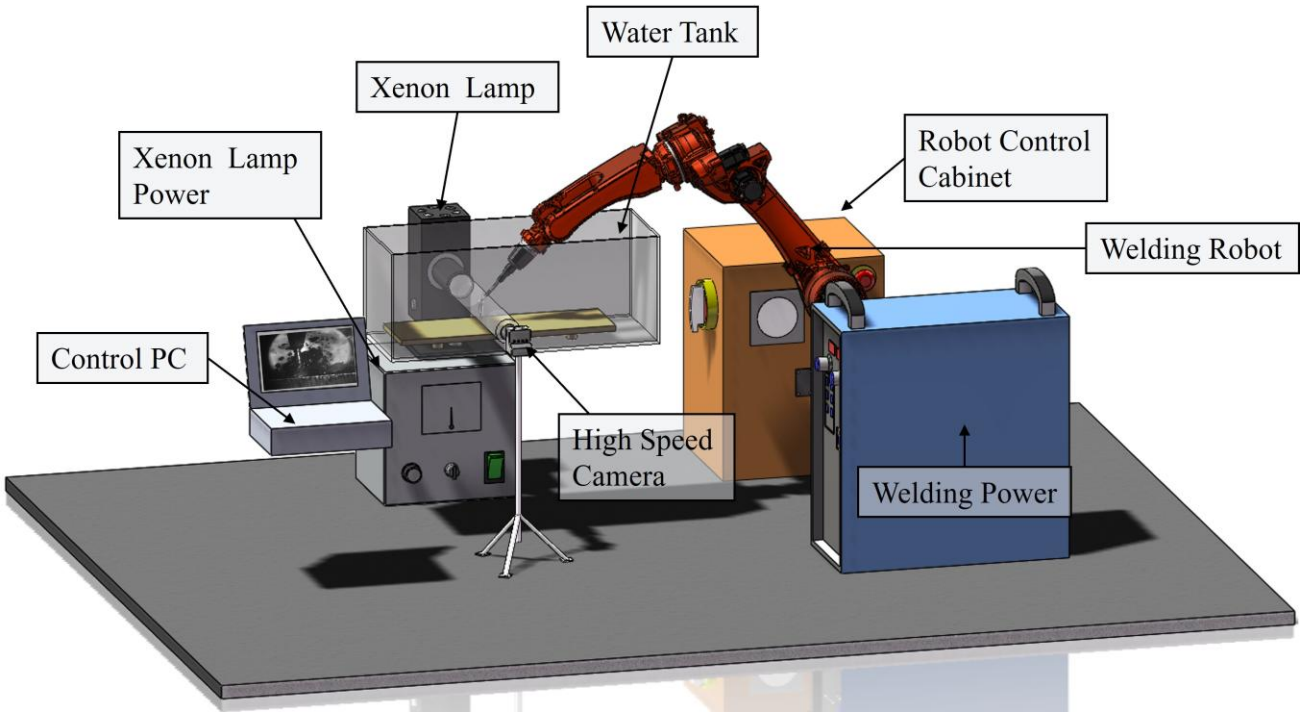


Fig. 1 Schematic diagram of the UWW system and its synchronized imaging and electrical signal monitoring

Depicted in Figure 1 are schematic representations of the underwater wet welding (UWW) system alongside the synchronized monitoring platform for both high-speed imaging and electrical signal recording. Part (a) shows the visible light acquisition setup, while part (b) depicts the electrical signal synchronous acquisition system. As indicated in Fig. 1(b), the acquisition box contains built-in Hall sensors for voltage and current, which are used to record voltage and current signals, respectively. The sampling rate for electrical signals is 20,000 Hz, meaning that ten sets of electrical signals are collected for each image frame. Each image corresponds to the first data set among the ten electrical signal data sets in each group. Since the data acquisition interval is relatively short, each image can be regarded as the result of the combined effect of the ten electrical signals in each group. ADC welding power source was used in the experiment, which was carried out at a rated water depth of 0.5 m. Figure 2 provides a schematic diagram of the arc region in underwater wet welding, illustrating the relative positions and morphological characteristics of the arc bubble, droplet, molten pool, welding wire, and base metal. The contact tip-to-work distance (CTWD) is specifically defined as the sum of the wire extension length and the arc column length. To evaluate the effects of welding parameters on arc bubble and arc stability indicators, a three-factor, three-level design was conducted. Based on the response surface methodology using the Box–Behnken design (BBD) model, experimental investigations were carried out on representative combinations of factor levels. The factors investigated were contact tip-to-work distance (CTWD), wire feed speed, and welding voltage. CTWD, wire feed speed, and welding voltage

are quantitative variables. Table 2 presents the input variables along with their respective high and low levels, and Table 3 presents the response surface experimental design of the factor combinations.

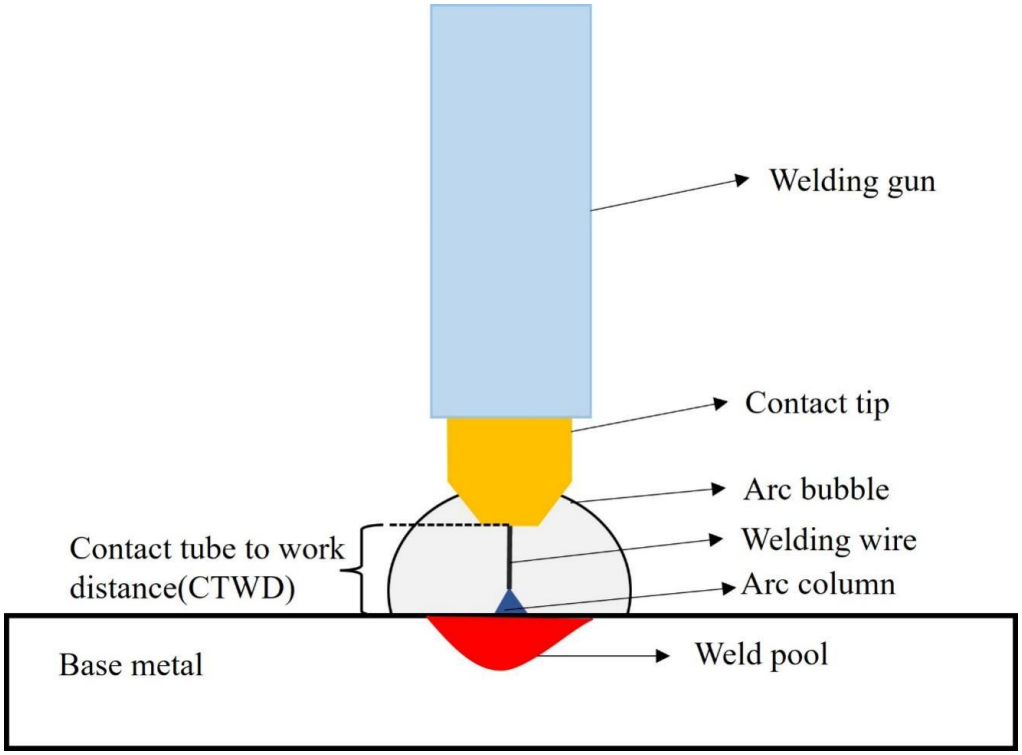


Fig. 2 Schematic diagram of the arc region in underwater wet welding

Table 2 Factors and levels for welding experiment

Parameters	Values		
	-1	0	+1
CTWD(mm)	12	16	20
Wire Speed(m/min)	4	5	6
Voltage(v)	26	30	34

Table 3 Response surface experimental design

No.	CTWD (mm)	Wire Speed (m/min)	Voltage (v)
1	12	5	26
2	12	5	34

3	12	4	30
4	12	6	30
5	16	6	34
6	16	5	30
7	16	5	30
8	16	5	30
9	16	5	30
10	16	5	30
11	16	4	26
12	16	4	34
13	16	6	26
14	20	6	30
15	20	4	30
16	20	5	26
17	20	5	34

3.Results and Discussion

3.1 Dynamic behavior of arc bubble during arc initiation in UWW

The arc initiation process is the initial stage of arc discharge, and the stability during the arc initiation stage in underwater wet welding significantly affects the subsequent weld formation quality. As shown in Fig. 3, at time t0, the wire tip contacts the base metal surface, causing a short circuit in the welding power source. The voltage rapidly drops from the open-circuit voltage of 80 V to 50 V, while the current rises sharply to the short-circuit current of 600 A. During the short circuit, the contact point generates substantial resistive heat due to the high current density, causing the surrounding water environment to rapidly heat up, vaporize, and decompose into hydrogen and oxygen plasma. Simultaneously, the wire tip begins to melt, and the base metal, acting as the cathode, starts to release electrons. Under the influence of the electric field, electrons acquire a high initial velocity and move toward the anode connected to the welding wire.

Charged particles undergo violent collisions with neutral gas atoms (molecules) in the gas space formed by the vaporization of the water environment. When an electron's collisional kinetic energy exceeds the ionization threshold

of the gas atoms, the impact is inelastic. This causes the ejection of an outer-shell electron from a neutral gas atom, thereby creating a free electron and a positive ion. The newly generated free electron repeats the motion process of the original electron and continues moving toward the anode at an extremely high velocity. This electron avalanche collision process causes the number of free electrons to increase exponentially, generating a large number of free electrons moving rapidly toward the wire tip in an extremely short time. Within the original gas space, an electron cloud dominated by free electrons forms at the front, while a conductive channel dominated by slowly moving positively charged ions forms at the rear. The additional electric field generated by this "electron cloud–conductive channel" model superimposes with the original electric field, enhancing the electric field strength in the gas space and further promoting the collision process. When the electron cloud reaches the anode connected to the wire tip and the positively charged ions reach the cathode base metal, a plasma-filled conductive channel is established. The gas space is completely broken down, the resistance drops sharply, the current increases instantaneously, and intense light and substantial heat are released, initiating the arc. The released heat continues to heat and vaporize the surrounding water environment, ultimately generating the underwater arc bubble.

After the arc initiation stage, the gaseous environment within the bubble reduces the heat exchange between the arc column and the surrounding environment. The heat released by arc combustion enhances the thermal motion of various particles in the gas space, allowing ionization to be completed solely through thermal collisions, thereby maintaining the stability of the electron channel and ensuring stable arc combustion without extinction. Figure 3 illustrates the growth process of the first arc bubble under the third set of welding parameters, along with the corresponding current and voltage variations. From t0 to t0+1.5 ms, the arc bubble radius continuously increases. At t0+1.5 ms, both the short-circuit current and instantaneous arc power reach their peak values, yet the arc bubble radius has not yet reached its maximum. At t0+4.0 ms, the bubble radius attains its maximum value. This may be attributed to the fact that at the moment of arc bubble generation, the enormous Joule heat produced by arc combustion causes the water environment to heat up and vaporize. A bubble will expand when the pressure of the gas within it is high enough to overcome the external hydrostatic pressure.As the bubble volume gradually increases, the internal pressure decreases. After reaching equilibrium, the internal and external pressures become equal; however, the outward expansion velocity of the bubble still exists. Due to inertia, the outward expansion trend does not cease immediately, and the bubble radius continues to increase until the outward expansion velocity decreases to zero, at which point the bubble reaches its maximum radius. At this moment, the internal gas pressure has already become lower than the external hydrostatic pressure, and the bubble begins to collapse under the pressure difference.

During the collapse stage, the top of the bubble collapses more rapidly, with a more pronounced collapsing phenomenon. The arc bubble gradually contracts from a hemispherical shape into a cone that is narrow at the top and wide at the bottom, as shown at t0+5.4 ms. As the bubble collapse progresses, the bubble shape transforms from a conical shape into a cylindrical gas column that rises upward. Between t0+5.4 ms and t0+7.1 ms, the bubble volume continuously decreases while the total amount of gas remains constant, resulting in an increased gas flow velocity within the bubble. Affected by buoyancy and exhibiting an upward floating tendency, the rapidly flowing gas disturbs the original ion channel, preventing free electrons emitted from the cathode from continuously and stably passing through the ion channel to reach the anode connected to the welding wire. This disturbance causes fluctuations in arc length and shape, ultimately leading to arc extinction.

Figure 4 illustrates the growth process of the first arc bubble under the second set of welding parameters, along with the corresponding current and voltage signal variations. It can be observed that during the growth stage, the morphological evolution is generally consistent with that shown in Fig. 3. However, during the collapse stage, due to the larger bubble radius and greater total internal gas volume, the rapid gas flow during collapse and upward floating causes more intense disturbances to the original ion channel within the bubble. It is precisely this intensified disturbance that results in two voltage peaks and one voltage trough during the period from t1+5.3 ms to t1+7.9 ms, ultimately leading to arc extinction. Compared with Fig. 3, the fluctuations in current and voltage signals under this set of parameters are significantly more severe. Therefore, as the maximum radius of the arc bubble during the arc initiation stage decreases, the total amount of gas within the bubble also decreases. During the bubble collapse stage, the influence of gas flow within the bubble on the arc is reduced, leading to smaller fluctuation amplitudes, which is more favorable for maintaining arc stability during the arc initiation stage.

Depicted in Fig. 5 are the bubble's expansion and subsequent collapse stages as observed during underwater wet welding. The arc bubble that forms around the welding zone creates a shielding environment that supports arc combustion and droplet transfer in underwater operations. For a more detailed examination of the bubble's growth and evolution during arc initiation, the coordinate origin is placed at the lowest point of the bubble, as shown in Fig. 5(b). The coordinate system is defined as follows: the X-axis runs transverse to the welding wire and parallel to the base plate, while the Y-axis follows the welding wire's longitudinal axis, with its positive direction directed upward (opposing gravity).To provide a more precise description of arc bubble behavior during the arc initiation phase in underwater wet welding, it is essential to analyze the bubble's edge contour size and growth rate at various θ angles. The specific measurement approach is depicted in Fig. 5(b). Figures 5(c) and (d) illustrate the morphological

evolution of the arc bubble during the collapse stage. At this stage, the bubble's morphology evolves from ellipsoidal to conical as its volume progressively declines. The shielding gas inside the bubble exhibits increasing flow velocity along the welding wire and the upper base metal surface, with approximate flow trajectories provided in Fig. 5(d).

Figure 6(a) shows the variation of bubble radius with time at different θ angles for the third set of parameters. From 0 to 4.5 ms, the bubble radius at different θ angles exhibits an increasing trend, reaching its maximum value at 4.5 ms. At this moment, as the θ angle increases, the bubble radius first increases and then decreases, with the maximum bubble radius occurring at approximately 30°. This finding indicates an ellipsoidal bubble morphology, with the X-axis dimension marginally greater than that measured along the Y-axis. Subsequently, the bubble undergoes collapse. At 7.5 ms, the Y-axis radius of the bubble shows a minor enlargement, a change attributable to buoyancy-induced upward motion of the bubble.

Figure 6(b) shows the variation of bubble growth rate with time at different θ angles. Positive values indicate growth along the radial direction. From 6 to 7 ms, the bubble collapse rates along the X-axis and Y-axis directions are significantly lower than those at other θ angles, and the arc bubble contour undergoes a notable transformation, evolving from an ellipsoidal shape into a conical shape growing along the Y-axis direction.

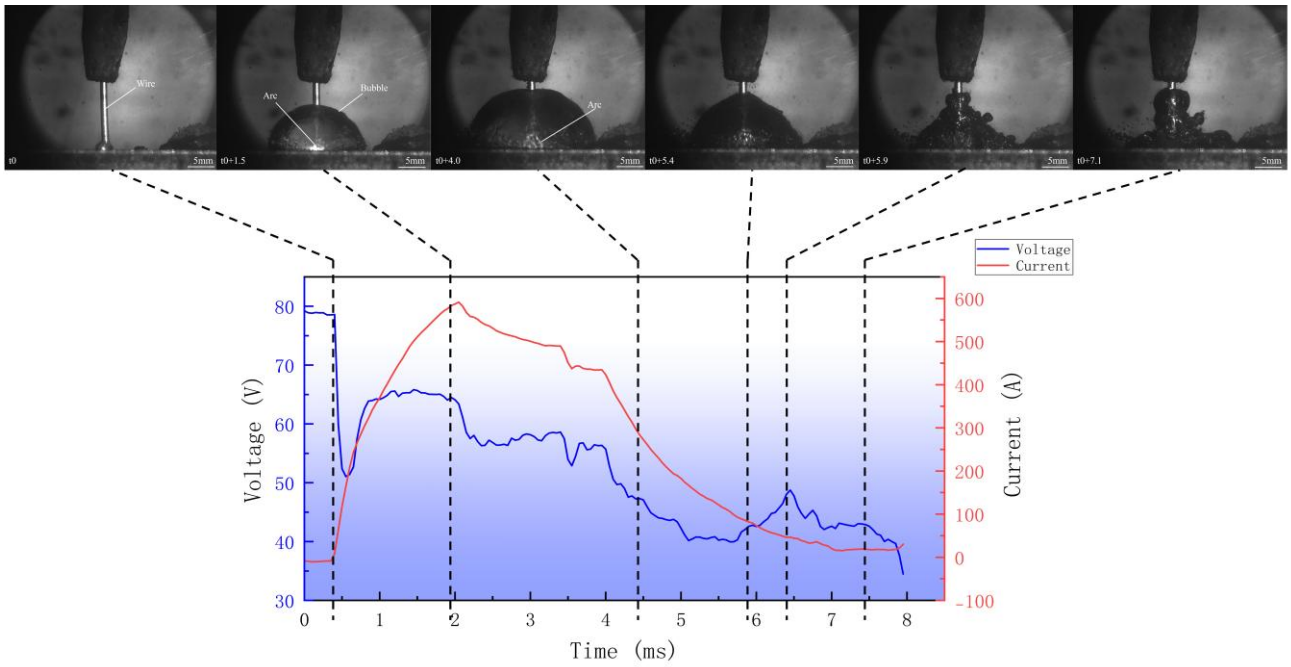


Fig. 3 High-speed camera images and welding electrical signals during the underwater arc initiation stage for Experiment Group 3

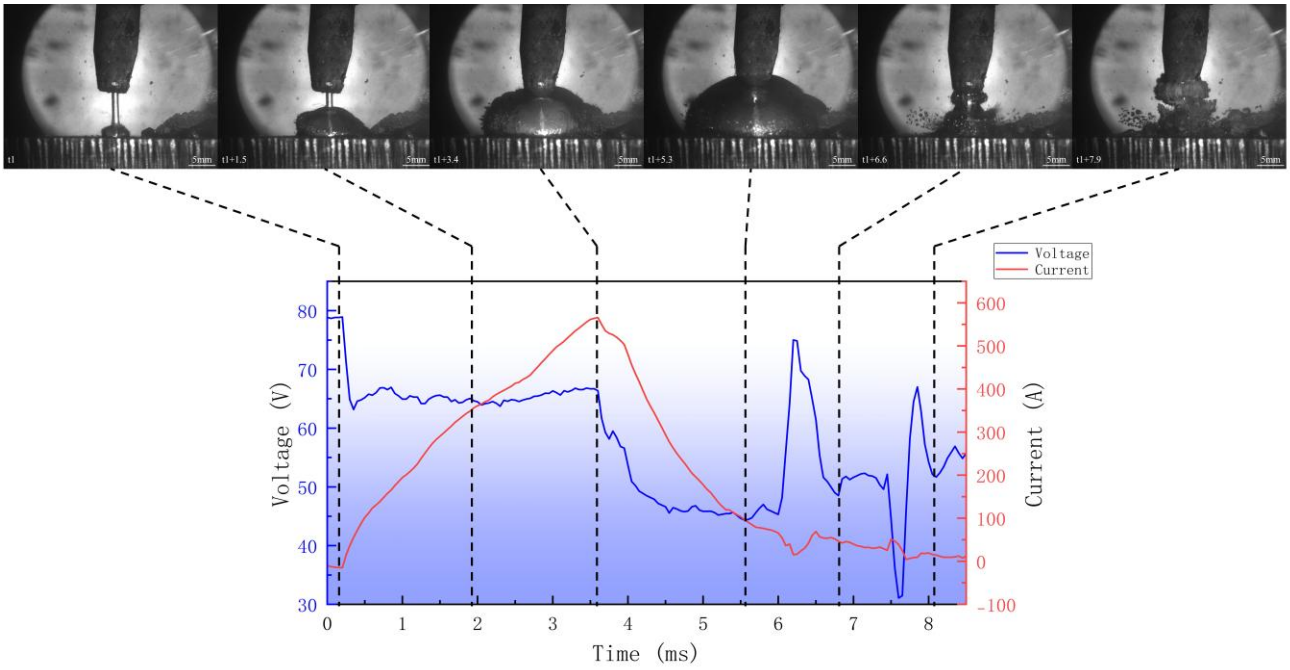


Fig. 4 High-speed camera images and welding electrical signals during the underwater arc initiation stage for Experiment Group 2

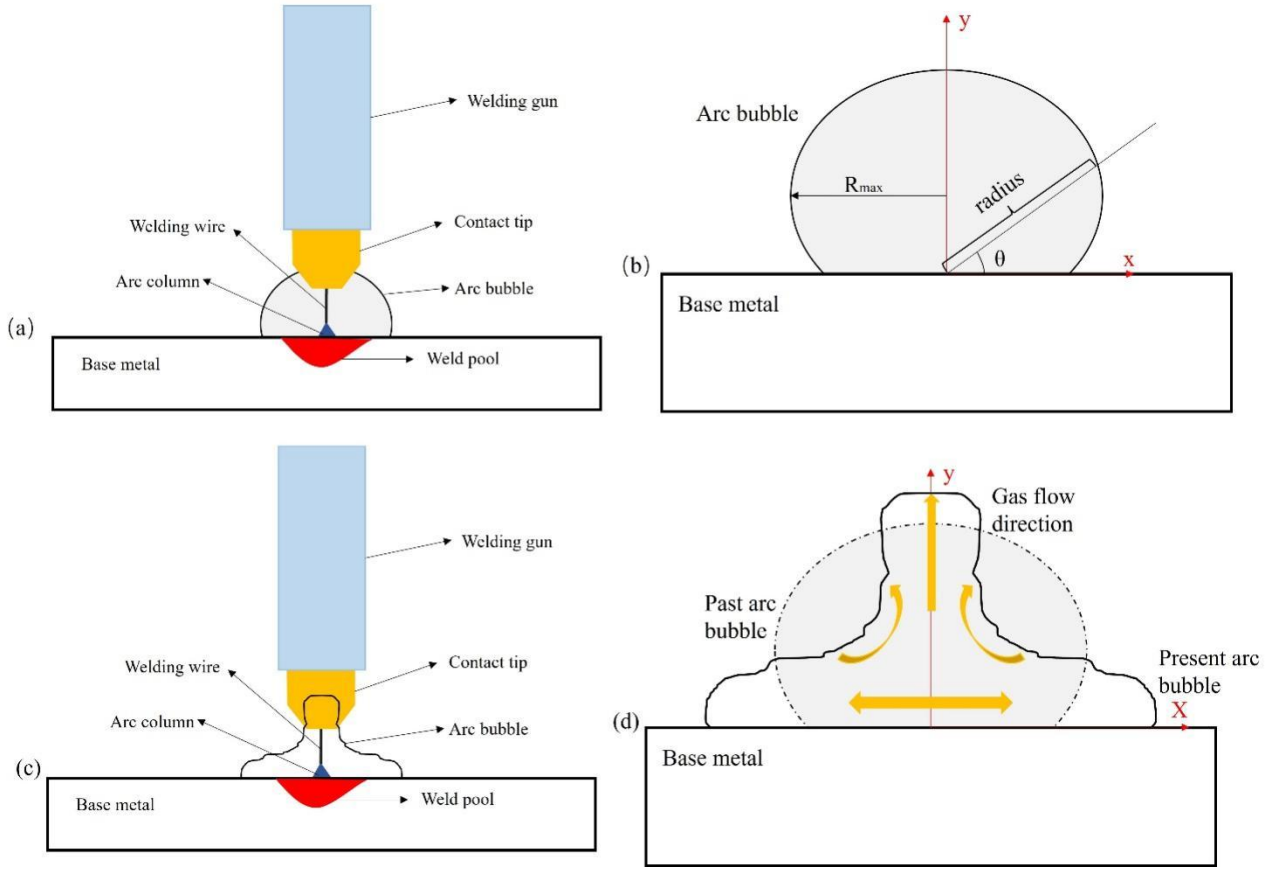


Fig. 5 (a), (b) Schematic diagrams of the arc bubble growth stage (c), (d) collapse stage

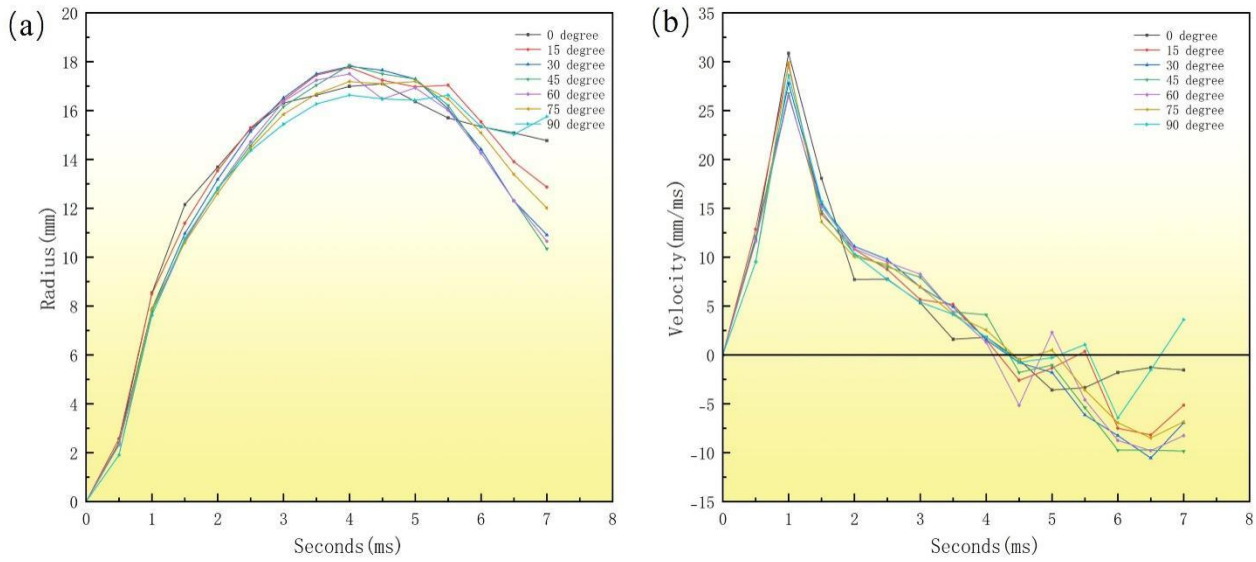


Fig. 6 (a) Bubble radius (b) bubble expansion rate at different angles

3.2 Response surface analysis

To optimize the arc bubble during the arc initiation stage, reduce its impact on arc stability, and improve weld formation quality, A Box–Behnken design (BBD)-based response surface approach was adopted for the systematic investigation of how CTWD, wire feed speed, and welding voltage affect the outcomes. The maximum bubble radius and bubble duration were selected as response variables. The initial experimental data were obtained from Table 4, which includes input features (CTWD, wire feed speed, and welding voltage) and output features (maximum bubble radius and bubble duration). In this study, relevant software was used to explore the effects of these parameters on the arc bubble during arc initiation, revealing the influence of the three factors on the response variables based on model fitting, and predicting the optimal conditions.

In mathematical modeling, R^2 is an important indicator used to measure the goodness of fit of the model to the data. The closer the R^2 value is to 1, the better the model fitting effect. By comparing the R^2 values of different models and the differences between the actual R^2 and the predicted R^2, the quadratic models for maximum bubble radius and bubble duration were ultimately selected. Equations (1) and (2) of the quadratic models respectively show the effects of individual factors (CTWD, wire feed speed, and welding voltage) and the interactions between any two factors on the response variables (maximum bubble radius and bubble duration). In the quadratic models, the R^2 for maximum bubble radius is 0.9950, and the R^2 for bubble duration is 0.9736. These high coefficients of determination (R^2) indicate an excellent model fit, confirming the accuracy of the model predictions.

Table 4 Raw data table

NO.	CTWD (mm)	Wire feed speed (m/min)	Voltage (V)	Max bubble radius(mm)	Bubble lifetime (ms)
1	12	5	26	18	8.35
2	12	5	34	17.4	7.75
3	12	4	30	15.2	7.60
4	12	6	30	15.9	7.10
5	16	6	34	17.6	7.00
6	16	5	30	15.2	7.40
7	16	5	30	15.3	7.44
8	16	5	30	15.3	7.40
9	16	5	30	15.2	7.52
10	16	5	30	15.2	7.45
11	16	4	26	16.5	8.05
12	16	4	34	16.6	7.65
13	16	6	26	16.1	7.00
14	20	6	30	16.2	6.50
15	20	4	30	16.3	7.35
16	20	5	26	17.6	7.35
17	20	4	34	19.7	7.70

Maximum bubble radiu = [+15.24+(0.4213×A)+(0.1500×B)+(0.3788×C)+(-0.2000×AB)+(0.6825×AC)+(0.3500×BC)+(1.06×A2)+(-0.4038×B2)+(1.86×C2)] (Ep 1)

Lifetime of Bubble = [+7.44+(-0.2125×A)+(-0.3563×B)+(-0.0812×C)+(-0.0875×AB)+(+0.2375×AC)+(+0.1000×BC)+(+0.0290×A2)+(-0.3335×B2)+(+0.3165×C2)] (Ep 2)

3.2.1 Analysis of variance (ANOVA)

ANOVA serves as a statistical tool for identifying significant differences across three or more variables. A P-value less than 0.05 is taken as statistically significant. Table 5 displays the ANOVA outcomes for the UWW arc initiation stage's maximum bubble radius. As seen in Table 5, the model yields an F-value of 357.34 and a P-value <0.0001, both indicating strong significance. The lack-of-fit test returns an F-value of 4.91 and a P-value of 0.0791, both relatively modest, implying good agreement between the data and the model. The Adjusted R^2 is close to unity, and the discrepancy between Adjusted R^2 and Predicted R^2 falls within 0.2. These outcomes collectively affirm the model's robust fit and its sound predictive accuracy concerning the maximum bubble radius during arc initiation under the prescribed parameters.In Table 5, the P-values for the individual factors CTWD (A) and Voltage (C) are both <0.0001, while the P-value for Wire feed speed (B) is 0.0021, indicating that under the effect of individual factors, CTWD and Voltage are the main factors influencing the maximum bubble radius, exhibiting significant effects. Under the interaction effects of any two factors, the interaction term (AC) and the quadratic terms (A^2, B^2, and C^2) all have P-values <0.0001 and high F-values, demonstrating the significant influence of these factors.

Figure 7 consists of a predicted vs. actual value plot (a) and a residual vs. run order plot (b). In Fig. 7(a), the solid line represents the line formed by the predicted values. Most of the actual observed points lie on the predicted line, with a small portion uniformly distributed on both sides close to the solid line, demonstrating that the model can accurately predict the maximum bubble radius. Residuals refer to the differences between observed values and actual values. In Fig. 7(b), the residuals are randomly distributed on both sides of the zero line, exhibiting a horizontal band-like distribution with small fluctuations, which further confirms the good fit of the model and its ability to accurately predict the response variables.

ANOVA results pertaining to bubble duration during UWW arc initiation are presented in Table 6. This table reveals a high F-value and a very low P-value for the model, whereas the lack-of-fit values (F and P) are relatively low—indicative of a strong data-model fit. The Adjusted R^2 approaches 1, and the discrepancy between Adjusted R^2 and Predicted R^2 remains below 0.2. These indicators collectively attest to the model's robust fit and sound predictive

accuracy for bubble duration under the given parameters. As for the influencing factors, CTWD (A) and wire feed speed (B), in addition to the quadratic terms B^2 and C^2, stand out as the principal determinants of bubble duration.

Figure 8 includes two plots: a predicted versus actual value plot (a) and a residual versus run order plot (b). Fig. 8(a) reveals a uniform, symmetric distribution of data points around the prediction line—a clear indication of the model's predictive power. Residuals (observed minus actual values) are displayed in Fig. 8(b), where they appear randomly scattered across the zero line. This random pattern takes the shape of a horizontal band with small fluctuations. Together, these observations support the model's good fit and its ability to accurately predict the response variables.

Table 5 ANOVA for maximum bubble radius

Source	Sum of Squares	df	Mean Square	F-value	P-value	
Model	25.83	9	2.87	357.34	＜0.0001	significant
A-CTWD	1.42	1	1.42	176.74	＜0.0001	significant
B-Wire feed speed	0.1800	1	0.1800	22.41	0.0021	
C-Voltage	1.15	1	1.15	142.88	＜0.0001	significant
AB	0.1600	1	0.1600	19.92	0.0029	
AC	1.86	1	1.86	231.97	＜0.0001	significant
BC	0.4900	1	0.4900	61.00	0.0001	
A2	4.76	1	4.76	593.18	＜0.0001	significant
B2	0.6864	1	0.6864	85.45	＜0.0001	significant
C2	14.63	1	14.63	1820.88	＜0.0001	significant
Lack of Fit	0.0442	3	0.0147	4.91	0.0791	Not significant
Adjusted R2	0.9950					
Predicted R2	0.9719					

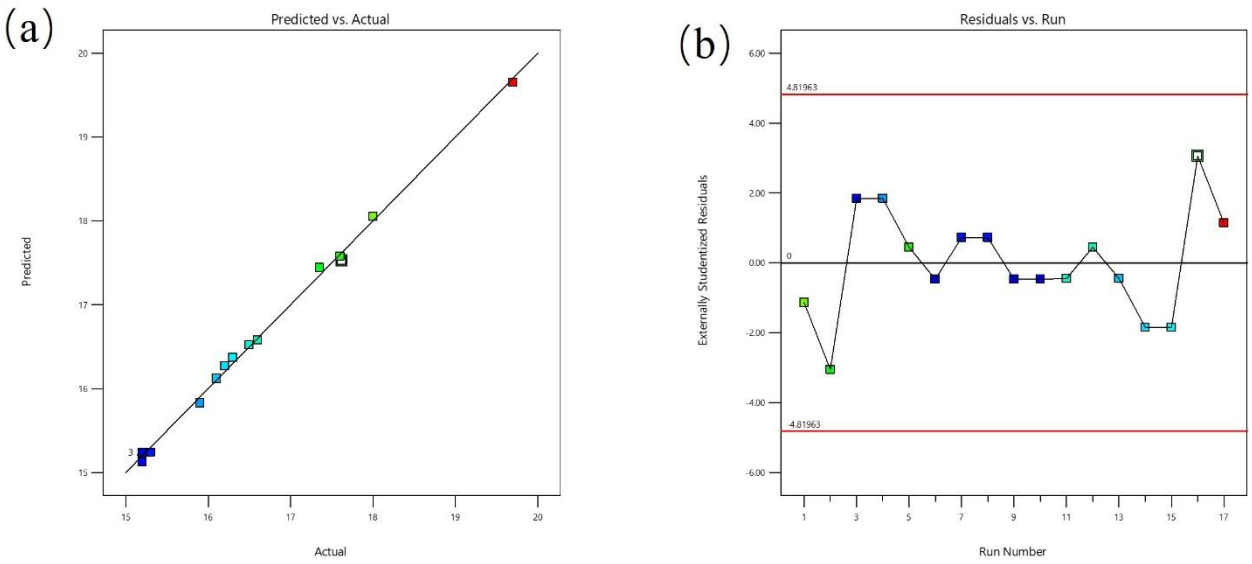


Fig. 7 (a) Predicted vs. actual plot (b) residuals vs. run order plot

Table 6 ANOVA for bubble duration

Source	Sum of Squares	df	Mean Square	F-value	P-value	
Model	2.81	9	0.3125	66.67	＜0.0001	significant
A-CTWD	0.4512	1	0.4512	96.26	＜0.0001	significant
B-Wire feed speed	1.16	1	1.16	248.12	＜0.0001	significant
C-Voltage	0.0528	1	0.0528	11.27	0.0121	
AB	0.0306	1	0.0306	6.53	0.0378	
AC	0.2256	1	0.2256	48.14	0.0002	
BC	0.0400	1	0.0400	8.54	0.0223	
A2	0.0035	1	0.0035	0.7556	0.4135	
B2	0.4683	1	0.4683	99.93	＜0.0001	significant
C2	0.4218	1	0.4218	90.00	＜0.0001	significant
Lack of Fit	0.0231	3	0.0077	3.19	0.1462	Not significant
Adjusted R2	0.9736					

Predicted R2	0.8646

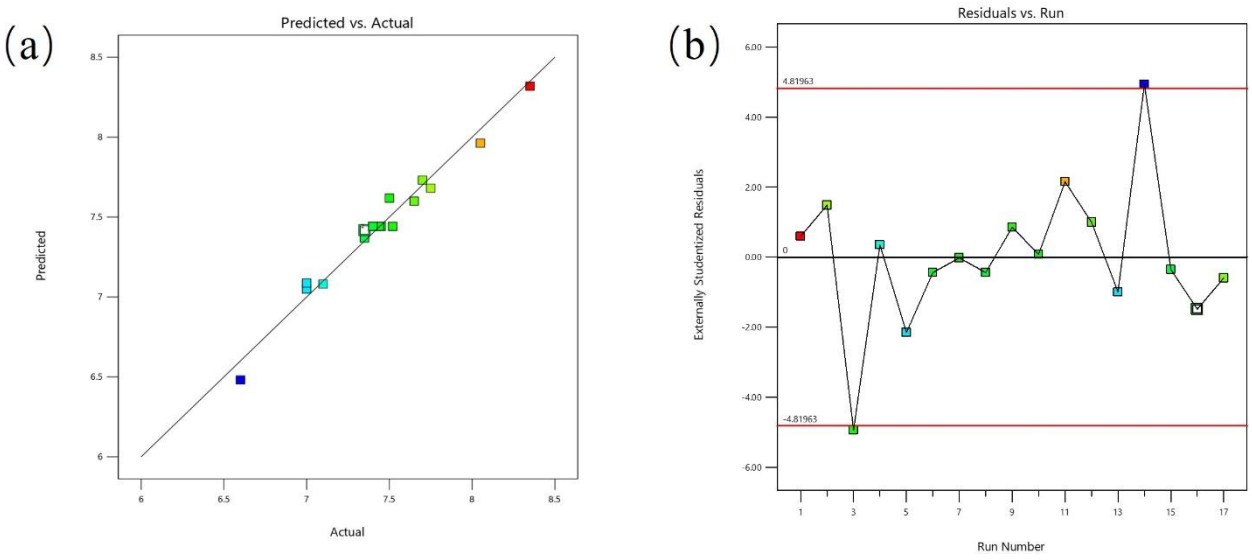


Fig. 8 (a)Predicted vs. actual plot (b) residuals vs. run order plot

3.2.2 Effects of multiple factors on maximum bubble radius and bubble duration

The response surface plots for maximum bubble radius and bubble duration are given in Figs. 9 and 10, respectively. These visualizations show how CTWD, wire feed speed, and welding voltage affect the two parameters during UWW arc initiation. Figure 9(a) specifically examines the relationship between wire feed speed, CTWD, and maximum bubble radius. Increasing wire feed speed from 4 to 6 m/min makes the maximum bubble radius first peak and then taper off; the optimal feed speed is around 5 m/min. In contrast, as CTWD ascends from 12 to 20 mm, the maximum bubble radius follows a distinct valley-shaped curve (first falling, then rising), with the optimum located at approximately 15 mm.

Figure 9(b) depicts how CTWD and welding voltage affect the maximum bubble radius. As CTWD increases, the maximum bubble radius first decreases and then increases, which is similar to the trend observed in Fig. 9(a), with the optimal value remaining at approximately 15 mm. Similarly, as welding voltage increases, the maximum bubble radius also exhibits a clear trend of first decreasing and then increasing, with the optimal welding voltage being approximately 30 V. Moreover, compared with the effect of CTWD variation on the maximum bubble radius, the trend induced by welding voltage variation is more pronounced, with a more significant difference between the peak and valley values.

The influence of wire feed speed and welding voltage on the maximum bubble radius is illustrated in Fig. 9(c). With an increase in wire feed speed, the maximum bubble radius rises to a peak at around 5 m/min and then declines slightly. As welding voltage increases, the maximum bubble radius similarly follows a clear decreasing-then-increasing pattern, bottoming out at a welding voltage of approximately 30 V. This trend is generally in agreement with that observed in Fig. 9(b).

Therefore, if only the maximum bubble radius is considered as a single response variable, based on the effects of the interactions among CTWD, wire feed speed, and welding voltage on this parameter as shown in Fig. 9, the optimal values for achieving the best bubble radius are CTWD of 15 mm, wire feed speed of 5 m/min, and welding voltage of 30 V.

Figure 10(a) shows the effect of the interaction between CTWD and wire feed speed on bubble duration. As CTWD increases, the bubble duration gradually decreases, exhibiting a monotonically decreasing trend. Meanwhile, as wire feed speed increases from 4 m/min to 6 m/min, the bubble duration first increases slightly, reaching a peak at approximately 4.3 m/min, and then decreases rapidly. This may be attributed to the fact that higher CTWD and higher wire feed speed result in a larger current at the moment of contact between the wire and the base metal during the arc initiation stage, leading to a substantial instantaneous heat input. This generates more welding gases (such as water vapor and hydrogen) per unit time, accelerating the bubble growth and collapse processes, making it difficult for the arc bubble to remain stable, and consequently resulting in a shorter bubble duration.

Figure 10(b) shows the effect of the interaction between welding voltage and CTWD on bubble duration. Increasing CTWD from 12 to 20 mm produces a steadily decreasing bubble duration, a trend that mirrors the results in Fig. 10(a). As for welding voltage, bubble duration decreases initially and then increases over the 26–34 V range, bottoming out at approximately 30 V.

Figure 10(c) demonstrates the interactive influence of wire feed speed and welding voltage on bubble duration. As wire feed speed rises, bubble duration climbs slightly to a peak around 4.3 m/min and then drops off rapidly. As for welding voltage, bubble duration shows an initial decline followed by an increase over the tested range. These findings are consistent with the patterns observed in Fig. 10(b).

Figure 11 shows the frequency distribution histograms of the maximum bubble radius and bubble duration, reflecting the central distribution trends of the two variables. Figure 11(a) shows the distribution of the maximum bubble radius, with the highest frequency occurring in the range of 15 mm to 16 mm. Figure 11(b) shows the

distribution of bubble duration, with the peak frequency located between 7 ms and 7.5 ms, indicating that most bubble durations fall within this range.

In summary, to achieve optimal maximum bubble radius and bubble duration during the arc initiation stage in underwater wet welding, the maximum bubble radius should be maintained as close as possible to the range of 15 mm to 16 mm, and the bubble duration should be kept within the range of 7 ms to 7.5 ms. Figure 12 shows the predicted optimal parameters under ideal conditions. Ultimately, a moderate CTWD (16 mm), a moderate wire feed speed (5 m/min), and a relatively high welding voltage (31 V) were selected. This combination of parameters yields relatively ideal values of 15.5 mm for the maximum bubble radius and 7.4 ms for the bubble duration.

Figure 12 shows the correspondence between the electrical signals and high-speed camera images during the arc initiation stage under the predicted welding parameters. To improve the comparability of the experimental results, the contact tip-to-work distance (CTWD) was set to 16 mm, the wire feed speed to 5.1 m/min, and the welding voltage to 31.0 V. The results show that no obvious fluctuations occurred in the electrical signals during the growth and collapse stages of the arc bubble. The current reached its peak at t0 + 3.5 ms, while the bubble radius reached its maximum value of approximately 15.6 mm at around t0 + 5.0 ms. The bubble duration was approximately 7.32 ms. These characteristics agree well with the predictions of the regression model, further verifying the accuracy of the model.

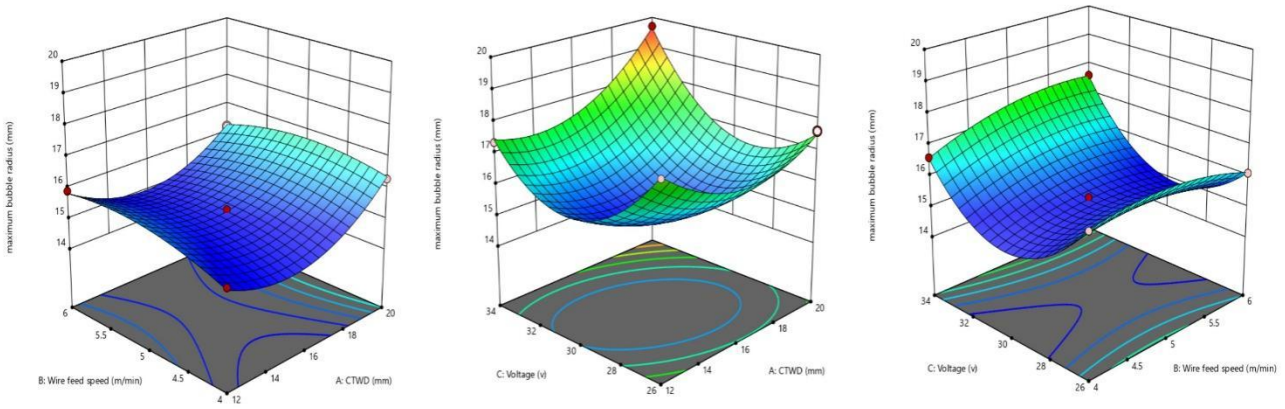


Fig. 9 Effects of the interaction between each pair of factors among welding voltage, wire feed speed, and CTWD on the maximum arc bubble radius

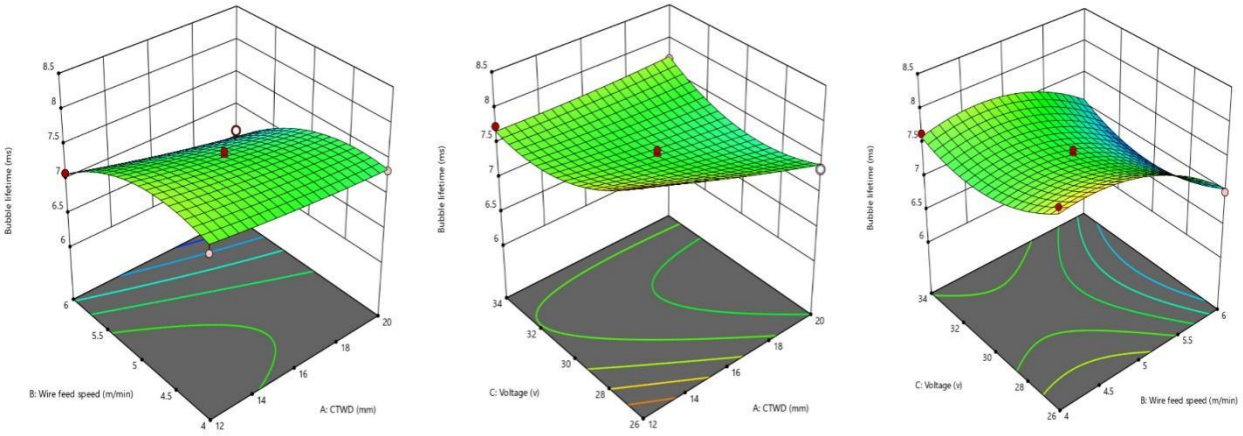


Fig. 10 Effects of the interaction between each pair of factors among welding voltage, wire feed speed, and CTWD on arc bubble duration

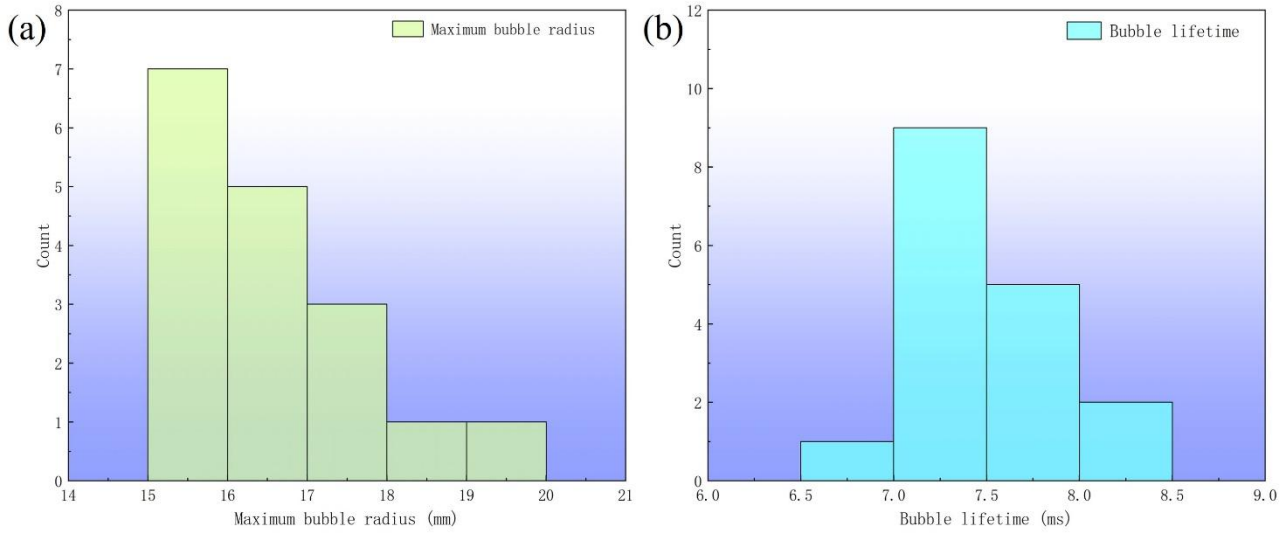


Fig. 11 Frequency distribution histogram

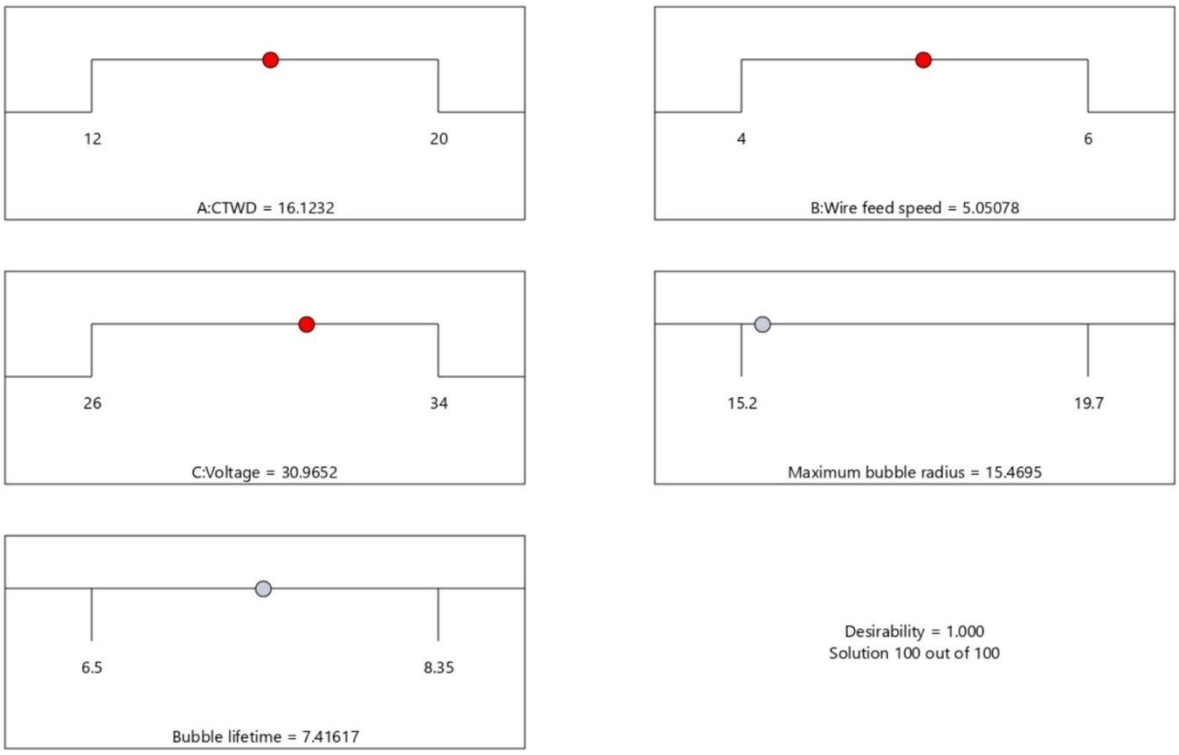


Fig. 12 Prediction of optimal parameters

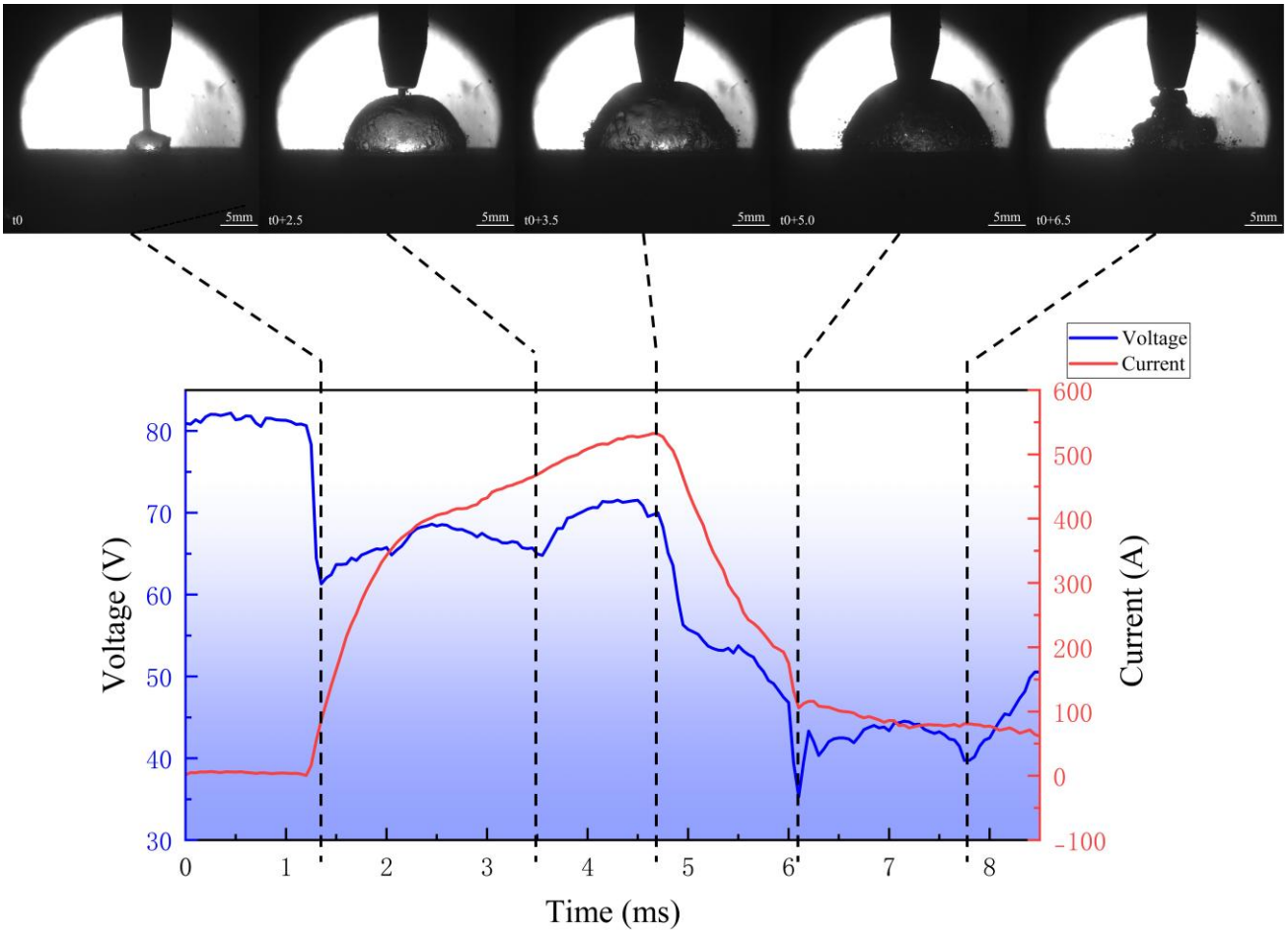


Fig. 13 High-speed camera images and welding electrical signals during the underwater arc initiation stage for the validation group

3.3 Analysis of welding electrical signals during the arc initiation stage

The welding electrical signals during the arc initiation stage in UWW are important indicators reflecting arc stability and have a profound impact on the subsequent welding process and final weld formation quality. Figure 14 shows the fluctuations of current and voltage signals during the arc initiation stage under different welding conditions, where (a), (b), (c), and (d) correspond to the electrical signal fluctuations under the welding conditions of Groups 1, 3, 13, and 17 in Table 4, respectively. To avoid the influence of unstable electrical signals in a short period of time on the analysis results and to eliminate contingency, the electrical signal graphs were all selected from the moment of arc initiation to 140 ms, when the current became relatively stable (for more details, refer to Supplementary Movie 1-4).

It is evident that the electrical signal waveforms vary considerably under different welding conditions. The signals shown in (a) and (d) display pronounced fluctuations, with multiple peaks appearing in both voltage and

current traces. This indicates that under the welding parameters of Groups 1 and 17, more frequent unstable arc events occurred during the arc initiation stage of UWW. The presence of instantaneous current peaks also points to the occurrence of short circuits. In (a), between 10 ms and 20 ms, a prolonged voltage peak accompanied by a current valley is observed following the initial fluctuation. This suggests that after the first arc bubble—generated at the moment of arc initiation—collapsed, an open circuit occurred, and the arc failed to re-establish successfully for an extended period.

Compared with (a) and (d), the electrical signal fluctuations in (b) and (c) show significant improvement, with the electrical signal fluctuations tending to stabilize and no prolonged short circuits or open circuits occurring, indicating a notable enhancement in arc stability. Variations in the maximum bubble radius during the arc initiation stage under different welding conditions may account for the significant differences observed in welding electrical signal fluctuations.The maximum bubble radii generated under the welding conditions corresponding to Fig. 14(a) and (d) (18 mm and 19.7 mm) are both larger than those generated under the conditions corresponding to Fig. 14(b) and (c) (15.2 mm and 16.1 mm). A larger bubble radius contains more welding gas internally. During the process in which the arc bubble contracts from a hemispherical shape to a conical shape and finally to a cylindrical gas column surrounding the welding wire, the bubble volume decreases, the internal gas flow velocity increases, and due to buoyancy, more gas flows upward. This causes the droplets, which should normally transfer to the underlying molten pool, to be disturbed by the gas flow and ejected in all directions, resulting in droplet spatter. At the same time, this gas flow disturbance also disrupts the stability of the arc channel formed by the original plasma, causing the originally stable arc to undergo significant oscillations, ultimately leading to large fluctuations in the welding electrical signals and a decrease in arc stability.

Previous studies have shown that the internal gas flow during bubble necking and collapse is one of the main sources of arc plasma perturbation [20-22]. Xu et al. reported that during the necking stage, the local gas velocity inside the bubble can reach approximately 274 m/s; severe necking can lead to arc extinction and is accompanied by temperature fluctuations exceeding 10 kK [22]. Cui et al. observed a localized perturbation region during the bubble necking stage in conventional underwater wet welding; this region reduces bubble stability and causes local arc temperature fluctuations [20]. In addition, Xu et al. pointed out that during the necking stage, the internal gas flow changes from a vortex flow to a concentrated upward flow, further perturbing the arc and droplets [21]. Since the amount of gas inside the bubble scales with R^3, a smaller bubble radius implies a smaller gas mass and lower collapse-induced gas jet kinetic energy. According to the aerodynamic force expression $F_b = 0.5\rho_g C_g u_0^2 \pi r_d^2$,

aerodynamic perturbation decreases with decreasing gas velocity [23]; Yang et al. also noted that the aerodynamic force inside the bubble can alter droplet and arc behavior [24]. Therefore, the above studies indicate that both the gas flow within the arc bubble and the dynamic behavior of the bubble have important effects on arc burning stability, providing strong support for the preceding analysis of arc bubble and electrical signal fluctuations during the arc initiation stage.

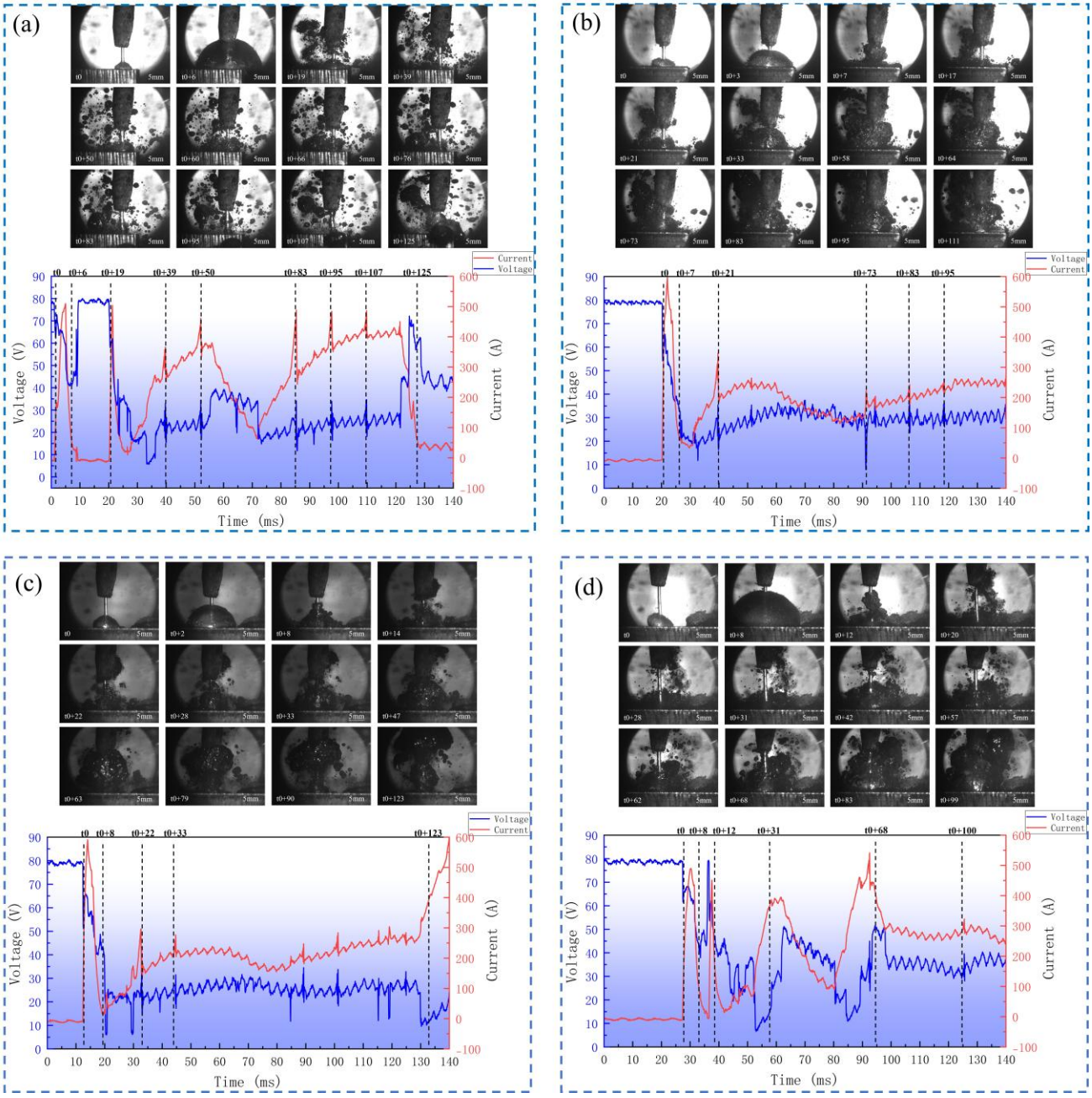


Fig. 14 Fluctuations of current and voltage signals during the arc initiation stage under different conditions: (a) Group 1, (b) Group 3, (c) Group 13, (d) Group 17

To facilitate a better assessment of arc stability, U-I scatter plots (arc voltage vs. welding current) were constructed under varying welding conditions, allowing the central distribution characteristics of the electrical signals to be identified. As illustrated in Fig. 15, these scatter plots depict voltage signals as a function of current signals, and the degree of scatter concentration indicates the level of arc stability during welding. When U exceeds 50 V, the resulting high voltage leads to an elongated arc length, making the arc stiffness more vulnerable to disturbances from bubbles; this can readily cause arc extinction and thus fails to maintain stable arc combustion. When U drops below 15 V, the welding wire tends to make contact with the base metal molten pool, leading to short circuits. Accordingly, using 15 V and 50 V as thresholds, Based on the voltage ranges, the regions in the figure fall into three main types: stable arc (15–50 V), arc extinction (U > 50 V), and short-circuit (U < 15 V).It can be observed that, compared with the scattered distribution of data points in the stable arc region in (a) and (d), the data points in (b) and (c) show a relatively concentrated distribution in the stable arc region. Moreover, Fewer scattered points appear in the arc extinction and short-circuit regions, whereas more are found in the stable arc zone. This shift points to diminished arc voltage and welding current fluctuations, coupled with a notable improvement in arc stability.

Figure 16(a) provides a summary of three key parameters—average current, average voltage, and current coefficient of variation—measured under varying welding conditions. The coefficient of variation can be used to describe the degree of signal fluctuation. In general, the coefficient of variation is inversely proportional to arc stability, meaning that a smaller coefficient of variation reflects more stable arc electrical signals, and it can be used as an indicator for quantitative analysis and evaluation of arc stability. Here, A, B, C, and D correspond to the statistical data under the welding conditions of Groups 1, 3, 13, and 17 in Table 4, respectively.

It can be observed that the current coefficients of variation for Groups B and C are 48.8% and 55.8%, respectively, both lower than those for Groups A and D, which are 90.9% and 70.1%. This indicates that under the welding conditions corresponding to Groups B and C, the stability of the welding current is significantly improved. Therefore, as the bubble radius during the arc initiation stage decreases, the coefficient of variation of the welding current decreases significantly, resulting in smaller fluctuations and better arc stability.

Figure 16(b) summarizes the relative frequencies of short-circuit, arc extinction, and unstable arc combustion events across different welding conditions. As the welding conditions vary, the proportions of these three events exhibit significant differences. It can be observed that under the welding conditions of Groups B and C, the proportions of short-circuit events, arc extinction events, and unstable arc combustion events are significantly lower than those in Groups A and D, with the minimum values occurring under the welding parameters corresponding to

Group B. The overall distribution trend is generally consistent with the trends observed in Figs. 14 and 15.

Thus, as the maximum bubble radius during the arc initiation stage decreases, the electrical signal fluctuations tend to stabilize, the coefficient of variation of the welding current decreases, and the proportion of unstable arc events also decreases. These findings indicate that a smaller bubble radius is more conducive to maintaining arc stability and improving welding quality.

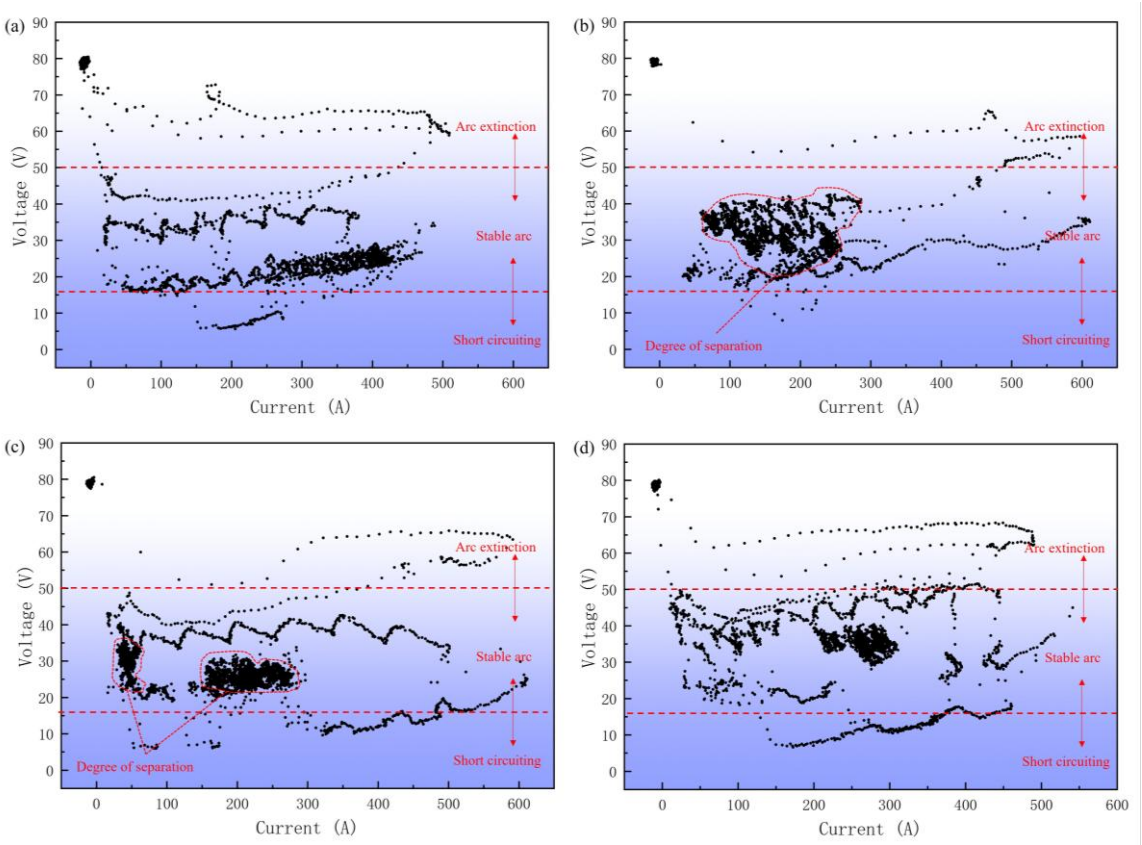


Fig. 15 Current-voltage scatter characteristics under diverse welding conditions:(a) Group 1, (b) Group 3, (c) Group 13, (d) Group 17

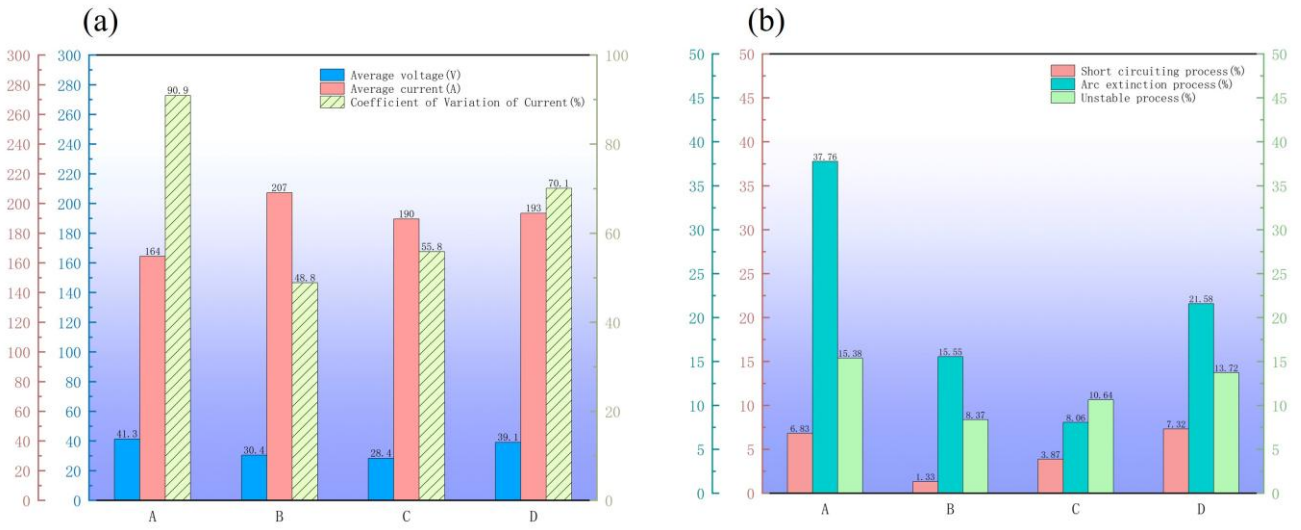


Fig. 16 Variation of welding current coefficient of variation (b) proportion of unstable arc region

3.4 Weld formation quality

Figure 16 shows the surface appearance of weld samples obtained under different experimental conditions. Combined with the above analysis, the maximum bubble radius during the arc initiation stage affects arc stability, which in turn influences weld formation quality. In Fig. 17, (a), (b), (c), and (d) correspond to the surface appearances of weld samples under the experimental conditions of Groups 1, 3, 13, and 17, respectively. The surface cavity defects in the weld samples of Groups (b) and (c) are slightly reduced compared with those in Groups (a) and (d), indicating an improvement in weld formation quality.

This may be attributed to the fact that under the experimental conditions of Groups (b) and (c), the electrical signal fluctuations tended to stabilize as both the current coefficient of variation and the proportion of unstable arc events dropped. This trend is more beneficial for securing a stable welding operation.According to the current and voltage signal fluctuations shown in Fig. 14, the number of short circuits occurring during the arc initiation stage in Groups (a) and (d) is significantly higher than that in Groups (b) and (c). High-frequency short circuits generate more droplet spatter, leading to a loss of weld metal quality, which in turn forms surface cavities of varying sizes on the weld surface, directly affecting weld formation quality.

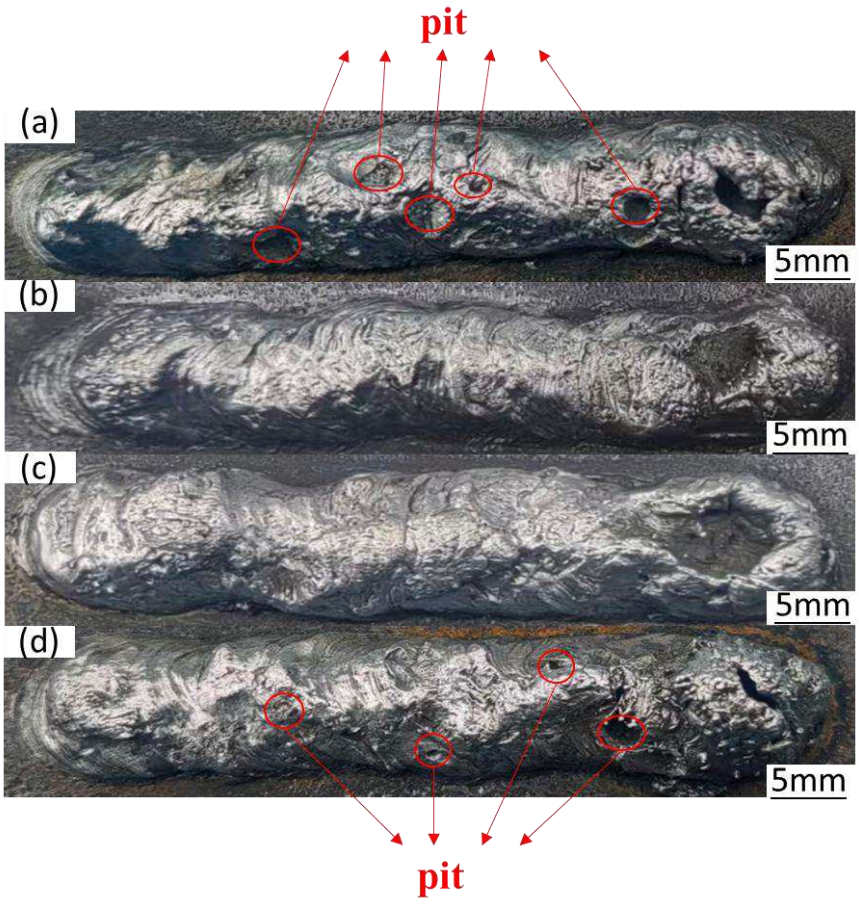


Fig. 17 Surface appearance of weld samples obtained under different experimental conditions

Figure 18 shows the variations in average weld width, average reinforcement, coefficient of variation of weld width, and coefficient of variation of reinforcement under different experimental conditions. The weld width is defined as the distance between the weld toes on the cross-section perpendicular to the welding direction, the distance between the intersections of the weld surface and the base metal. The weld reinforcement refers to the height of the weld metal protruding above the top surface of the base metal. The specific measurement methods for the weld width and reinforcement are shown in Fig. 18(b). Twenty data points were collected from each of the four groups of weld samples for statistical analysis, with one data point taken every 2 mm to ensure the universality and accuracy of the data. The results show that under the experimental conditions of Group 3, the average weld width and average reinforcement are 10.86 mm and 4.02 mm, respectively, which are relatively small. Under the welding conditions of Group 13, larger average weld width and average reinforcement of 12.15 mm and 5.4 mm, respectively, were observed.

The degree of fluctuation in weld sample surface dimensions can be measured using the coefficient of variation for both weld width and reinforcement. A lower coefficient signifies less dimensional scatter, a smoother surface

profile, and enhanced formation quality. For illustration, Groups 3 and 13 yield weld width coefficients of variation of 10.91% and 6.49%, respectively.Compared with Group 1 (9.23%) and Group 17 (9.87%), the weld width fluctuation in Group 13 is reduced. In terms of reinforcement, the coefficients of variation for Groups 3 and 13 are 10.97% and 12.35%, respectively, which are significantly lower than those of Group 1 (13.53%) and Group 17 (29.17%), indicating that the reinforcement dimensions in Groups 3 and 13 are more stable. Overall, when using the welding parameters of Groups 3 and 13, the weld formation quality is significantly better than that of Groups 1 and 17, with both weld width and reinforcement fluctuations being notably reduced.

Figure 20(a)–(d) present the instantaneous thermal power curves during the arc initiation stage for Groups 1, 3, 13, and 17, respectively, over a time range of 0–140 ms, consistent with Figure 13. Figure 20(e) shows the heat input per unit length and the coefficient of variation of thermal power during the arc initiation stage under the four parameter sets; the detailed calculation procedures are given in Eqs. (3) and (4). The data indicate that Groups 1 and 17 exhibited relatively high heat input per unit length and coefficient of variation of thermal power, leading to the formation of relatively large arc bubbles during the arc initiation stage. The enhanced perturbation of the arc by large bubbles induced strong electrical signal fluctuations, making the instantaneous thermal power highly unstable. In contrast, Groups 3 and 13 had slightly lower heat input per unit length, but their coefficient of variation of thermal power was significantly reduced. The stability of the instantaneous thermal power was therefore significantly improved, maintaining relatively stable heat input during the arc initiation stage. The above variation trend of thermal power is mutually corroborated by the metallographic morphologies of the heat-affected zone and weld zone under the four parameter sets in Figure 19, further explaining the intrinsic relationship between the differences in metal microstructure and the magnitude and stability of heat input during welding.

$$P(t)=U(t)I(t) \quad \text{(Ep3)}$$

$$Q=\frac{\int_{t_1}^{t_2} U(t)I(t)dt}{v(t_2-t_1)} \quad \text{(Ep4)}$$

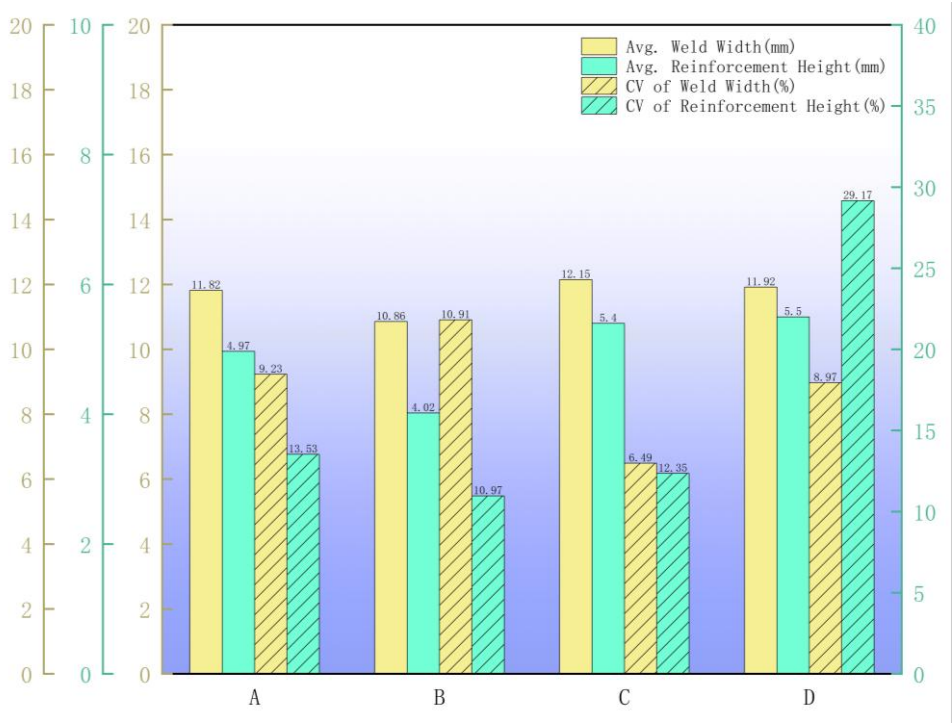


Fig. 18 Statistical chart of weld surface dimensional variations under different experimental conditions

Figure 19(a) shows a schematic of the weld morphology, in which the blue shaded region indicates the sampling location and range for metallographic observation. To ensure the consistency and accuracy of the measurement results, the sampling location was set at 10 mm from the starting end of the weld, with a sampling width of 10 mm. Figure 19(b) shows the weld cross-section, in which the blue and green boxes delineate the observation regions for the metallographic structures shown in Figures 18(c) and (d), respectively.

In Figure 19(c), c1, c2, c3, and c4 correspond to the metallographic structures of the heat-affected zones of the welds from Groups 1, 3, 13, and 17, respectively, and their microstructures are dominated by lath martensite. Among them, a small amount of acicular martensite is visible in c1 and c4, and an obvious crack defect is present at the fusion line in c1. It is considered that this crack originates from the large electrical signal fluctuations under the welding parameters of Group 1, where the instantaneous thermal power varies significantly with time and a stable heat input cannot be maintained, thereby resulting in a crack defect at the fusion line. In contrast, obvious diffusion layers appear in c2 and c3, which is attributed to the smaller arc bubble volume under the parameters of Groups 3 and 13. This weakens the perturbation effect on the arc during the arc initiation stage and reduces the degree of electrical signal fluctuation, thereby maintaining a relatively stable heat input over a prolonged period.

In Figure 19(d), d1 to d4 show the metallographic structures of the weld metal for the corresponding groups,

with austenite and ferrite as the main phases. Among them, the austenite grains in d2 and d3 are obviously coarse and exhibit a columnar grain morphology. This is because under stable heat input conditions, the cooling rate of the weld metal decreases and the nucleation rate decreases, which is favorable for grain growth and ultimately leads to the formation of larger columnar grains.

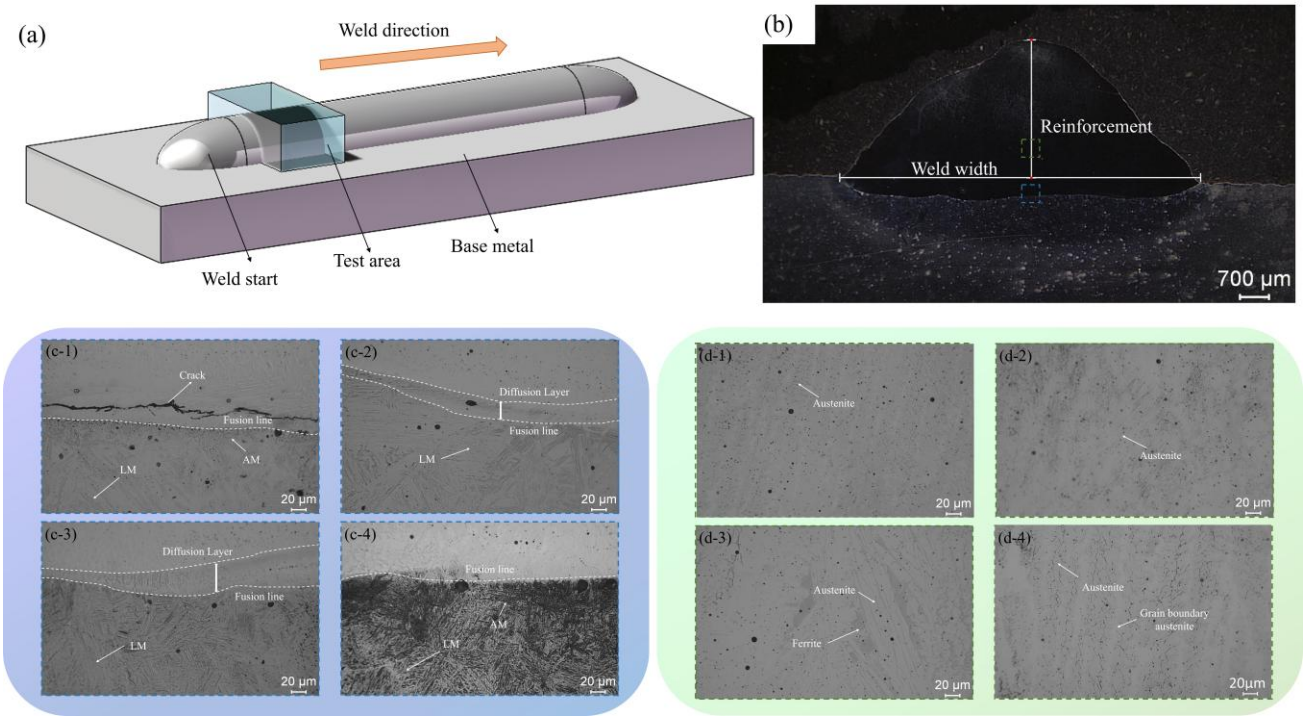


Fig. 19. (a) Schematic of the weld; (b) cross-sectional view of the weld; (c) microstructure of the heat-affected zone; (d) microstructure of the weld zone

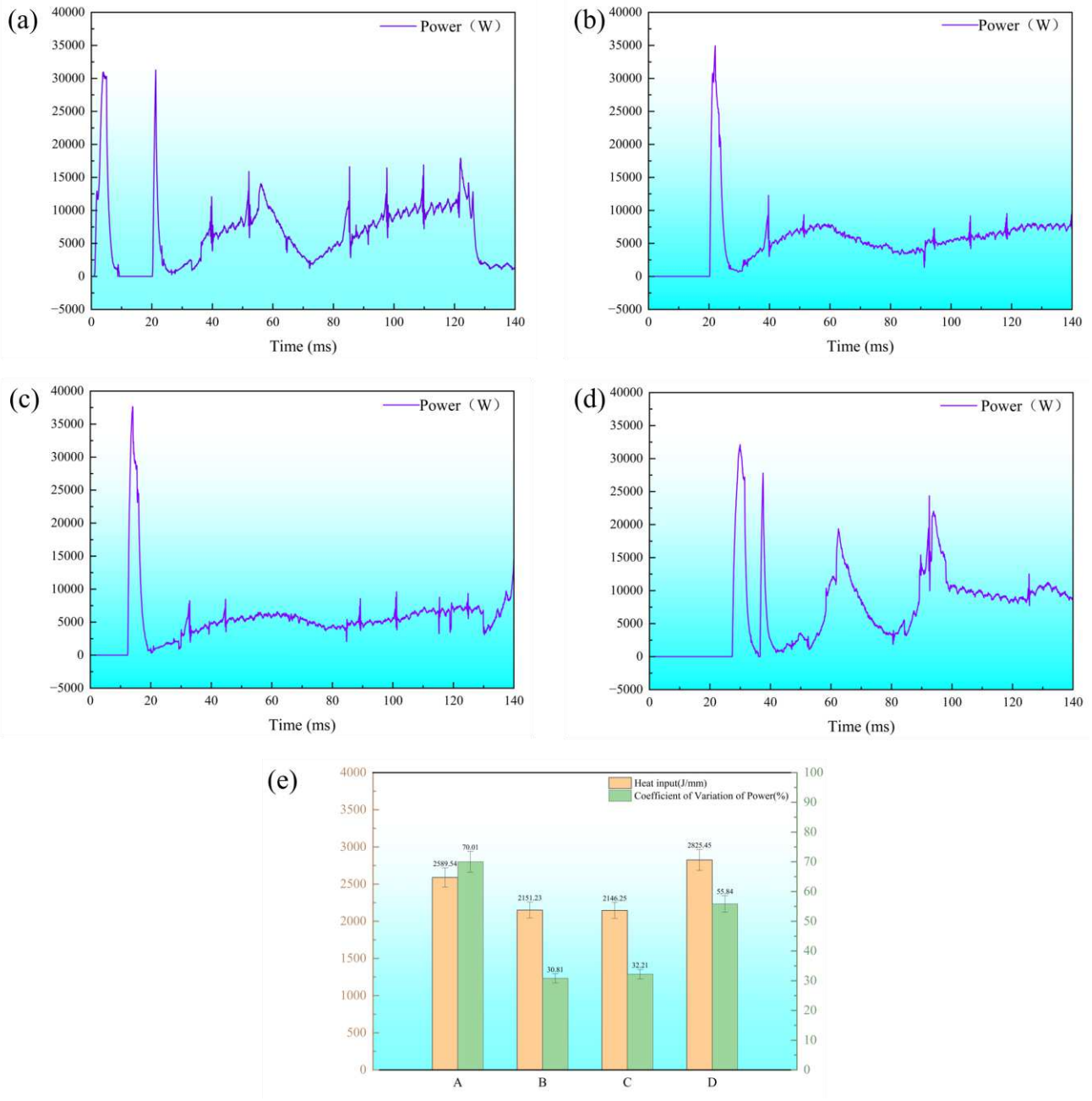


Fig. 20. Instantaneous thermal power during the arc initiation stage: (a) Group 1, (b) Group 3, (c) Group 13, (d) Group 17; (e) heat input per unit length and coefficient of variation of thermal power

Figure 21 shows the hardness distributions of the weld cross-sections of four specimens, with a data acquisition interval of 0.5 mm. Figure 21(a) presents the transverse hardness distribution of the weld, which generally exhibits an “M” shape, and its two peak regions correspond to the heat-affected zone (HAZ). This is attributed to the fact that the microstructure of the HAZ is dominated by lath martensite, whose hardness is significantly higher than that of the weld metal and the base metal. The hardness values of all four welds exceed 200 HV, which is higher than that of the base metal (140 HV). Figure 21(b) shows the longitudinal hardness test results along the weld centerline in the

direction perpendicular to the fusion line. The hardness distribution trends of the specimens are roughly the same, and the peak positions likewise correspond to the hardness of the HAZ.

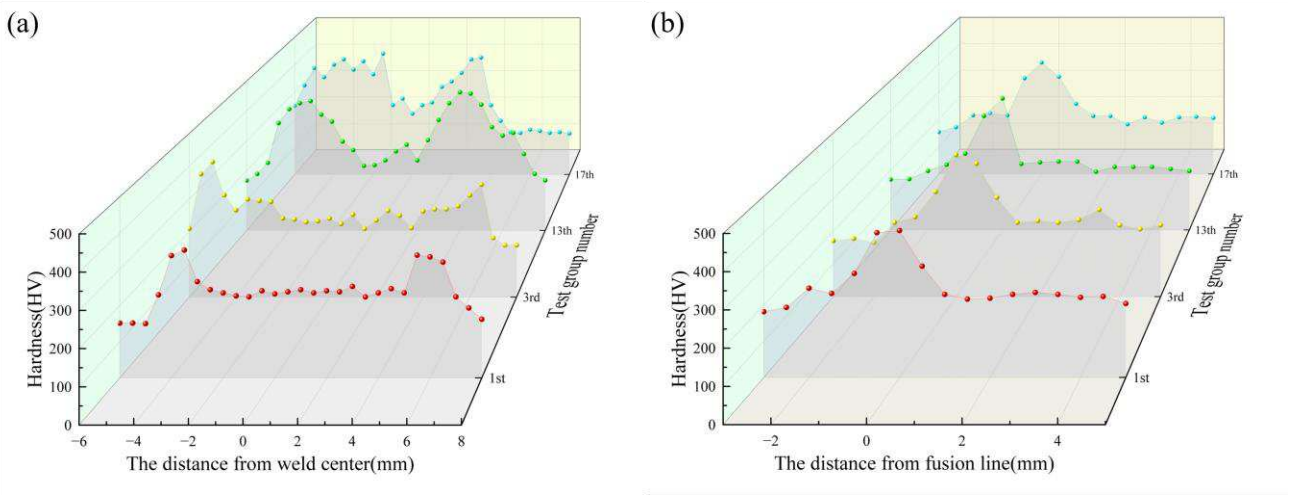


Fig. 21. Hardness distribution of the weld cross-section: (a) transverse hardness distribution; (b) longitudinal hardness distribution

4. Conclusions

This paper investigated the influence of CTWD, wire feed speed, and welding voltage on arc bubble dynamics and arc stability during underwater wet welding (UWW) arc initiation. A synchronized imaging/electrical signal acquisition system and a Box–Behnken design (BBD) response surface methodology were applied for this purpose. The main conclusions can be stated as follows:

(1) There are significant differences between the growth and collapse processes of the arc bubble during the arc initiation stage in wet welding. During the bubble growth stage, the extension rates at different θ angles are nearly identical, with the growth rate parallel to the base metal surface being slightly higher than that in the vertical direction, resulting in an ellipsoidal expansion along the direction parallel to the base metal surface. However, during the collapse stage, significant differences in collapse rates are observed at different θ angles, with the collapse rates at 0° and 90° being significantly lower than those at other angles, and the arc bubble evolves from an ellipsoidal shape into a conical shape in the vertical direction.

(2) CTWD, wire feed speed, and welding voltage each exert a significant influence on arc bubble maximum radius and duration during the arc initiation stage of underwater wet welding. Applying BBD-based response surface methodology yielded the following findings. When CTWD is increased, the maximum bubble radius follows a

quadratic trend—decreasing to a minimum near 15 mm before rising—while bubble duration exhibits a steady decrease. Increasing wire feed speed causes both bubble radius and duration to initially rise and subsequently fall. Increasing welding voltage produces a similar initial decrease followed by an increase in both parameters.

(3) During the arc initiation stage of underwater wet welding, the maximum bubble radius is one of the key factors affecting arc stability. As the maximum bubble radius decreased from 18 mm to 15.2 mm, the coefficient of variation of the current decreased to 48.8%, and the proportion of unstable arc events decreased to 8.37%. This improvement can be attributed to the smaller amount of welding gas contained in a smaller bubble. Consequently, during the bubble rising stage, the disturbance of the gas flow to the ion channel that sustains arc combustion is reduced, which helps maintain the stability of the ion channel to a certain extent and thereby improves arc stability.

(4) Final weld formation quality depends on arc stability during the arc initiation stage. Groups 3 and 13 yielded weld surfaces with fewer cavity defects and smaller coefficients of variation for both weld width and reinforcement, indicating a smoother surface and better bead geometry. In addition, clear fusion lines were observed in the weld microstructure of these two groups, indicating good metallurgical bonding between the weld metal and the base metal. The primary reason for this improvement lies in the conditions of these two groups: fewer short circuits occurred during arc initiation, and the arc burned more stably. As a result, droplet spatter-induced degradation of weld metal quality was lessened, and the occurrence of surface cavity defects was suppressed. Meanwhile, the stable arc burning provided a stable heat input, thereby promoting more sufficient fusion between the base metal and the weld metal.

Declaration of competing interest

The authors declare that they have no known competing financial interests or personal relationships that could have appeared to influence the work reported in this paper.

Contributions

Ziyang Lu: Writing – original draft, Investigation, Data curation. Hao Chen: Writing – review & editing, Methodology, Supervision, Funding acquisition. Zhengxian Liu:Writing – review & editing, Methodology. Rui Xi:Formal analysis, Lerong Zhao: Data curation. Chenyi Yan: Data curation. Zeshi Jin:Conceptualization, Resources. Feng Yu: Validation.

Acknowledgment

This work was supported by Funded by Science Research Project of Hebei Education Department (Grant No. QN2026137), National Natural Science Foundation of China (NNSFC) (Grant No.52105404).

Data availability

Data will be made available on request.

References

[1] Rowe M, Liu S (2001) Recent developments in underwater wet welding. Sci Technol Weld Join 6:387-396. https://doi.org/10.1179/stw.2001.6.6.387

[2] Świerczyńska A, Fydrych D, Rogalski G (2017) Diffusible hydrogen management in underwater wet self-shielded flux cored arc welding. Int J Hydrogen Energy 42:24532-24540. https://doi.org/10.1016/j.ijhydene.2017.07.225

[3] Zhang R, Chen H (2026) Research on arc oscillation promoting mass transfer and metal deposition forming in underwater wet welding processes. Mater Today Commun 50:114593. https://doi.org/10.1016/j.mtcomm.2025.114593

[4] Hu Y, Shi Y, Sun K, Shen X (2019) Microstructure evolution and mechanical performance of underwater local dry welded DSS metals at various simulated water depths. J Mater Process Technol 264:366-376. https://doi.org/10.1016/j.jmatprotec.2018.09.023

[5] Wang J, Sun Q, Hou S, Zhang T, Jin P, Feng J (2019) Dynamic control of current and voltage waveforms and droplet transfer for ultrasonic-wave-assisted underwater wet welding. Mater Des 181:108051. https://doi.org/10.1016/j.matdes.2019.108051

[6] Zhang M, Han Y, Jia C, Zheng Z, Li H, Wu C (2022) Improving the microstructures and mechanical properties with nano-Al2O3 treated wire in underwater submerged arc welding. J Manuf Process 74:40-51. https://doi.org/10.1016/j.jmapro.2021.11.056

[7] Guo N, Xu C, Du Y, Wang M, Feng J, Deng ZQ, Tang DY (2016) Effect of boric acid concentration on the arc stability in underwater wet welding. J Mater Process Technol 229:244-252. https://doi.org/10.1016/j.jmatprotec.2015.09.028

[8] Sun QJ, Cheng WQ, Liu YB, Wang JF, Cai CW, Feng JC (2016) Microstructure and mechanical properties of ultrasonic assisted underwater wet welding joints. Mater Des 103:63-70. https://doi.org/10.1016/j.matdes.2016.04.019

[9] Rogalski G, Świerczyńska A, Fydrych D (2023) Determination of t8/5 cooling times for underwater local dry welding of steel. Mar Struct 91:103477. https://doi.org/10.1016/j.marstruc.2023.103477

[10] Liao H, Kuang Y, Li X, Du W, Cheng L, Zhang Q, et al. (2026) Microstructure evolution of underwater welded SUS304 revealed by high-energy synchrotron-XRD. Int J Mech Sci 312:111284. https://doi.org/10.1016/j.ijmecsci.2026.111284

[11] Yang Q, Han Y, Jia C, Dong S, Wu C (2020) Visual investigation on the arc burning behaviors and features in underwater wet FCAW. J Offshore Mech Arct Eng 142:041401. https://doi.org/10.1115/1.4045914

[12] Feng J, Wang J, Sun Q, Zhao H, Wu L, Xu P (2017) Investigation on dynamic behaviors of bubble evolution in underwater wet flux-cored arc welding. J Manuf Process 28:156-167. https://doi.org/10.1016/j.jmapro.2017.06.003

[13] Chen H, Guo N, Huang L, Zhang X, Feng J, Wang G (2019) Effects of arc bubble behaviors and characteristics on droplet transfer in underwater wet welding using in-situ imaging method. Mater Des 170:107696. https://doi.org/10.1016/j.matdes.2019.107696

[14] Zhang X, Luo W, Zhang C, Yan K, Huang H, Chen H, et al. (2026) Motion characteristics and physical-property-driven formation mechanism of the molten-slag-covering mode in underwater wet flux-cored arc welding. J Mater Process Technol :119549.

[15] Chen J, Yang Q, Liu Z, et al. (2024) Dynamic behavior regulation of droplet transfer based on arc-bubble control by ultrasound-induced during underwater wet welding. J Manuf Process 129:147-160. https://doi.org/10.1016/j.jmapro.2024.08.050

[16] Chen J, Zhao J, Fu Q, et al. (2025) Impact of ultrasonic radiator end face geometry on dynamic behavior regulation of arc bubbles and arc stability in underwater wet welding. J Manuf Process 149:207-228. https://doi.org/10.1016/j.jmapro.2025.05.059

[17] Wang J, Sun Q, Ma J, Jin P, Sun T, Feng J (2019) Correlation between wire feed speed and external mechanical constraint for enhanced process stability in underwater wet flux-cored arc welding. Proc Inst Mech Eng Part B J Eng Manuf 233:2061-2073. https://doi.org/10.1177/0954405418811783

[18] Wang J, Sun Q, Zhang S, Wang C, Wu L, Feng J (2018) Characterization of the underwater welding arc bubble through a visual sensing method. J Mater Process Technol 251:95-108. https://doi.org/10.1016/j.jmatprotec.2017.08.019

[19] Yang Q, Dong Y, Zhang R, et al. (2025) Effects of spatial welding positions on arc bubble behavior, droplet transfer process, and weld microstructure and properties in underwater wet welding. J Manuf Process 135:46-68. https://doi.org/10.1016/j.jmapro.2025.01.030

[20] Cui X, Chen J, Zheng T, Su H, Li S, Wu C (2025) Experimental and simulation research on the dynamic behavior of arc and bubble in ultrasonic frequency pulse current-assisted underwater wet flux cored arc welding. Int J Heat Mass Transfer 242:126853. https://doi.org/10.1016/j.ijheatmasstransfer.2025.126853

[21] Xu S, Jia C, Maksymov S, Cai Z, Wu C (2024) Modeling the coupled bubble-arc-droplet evolution in underwater flux-cored arc welding. Int J Mech Sci 284:109754. https://doi.org/10.1016/j.ijmecsci.2024.109754

[22] Xu S, Jia C, Maksymov S, Wu C, Murphy AB (2025) Numerical investigation of the physical field evolution and coupled bubble-arc-droplet interactions in underwater wet flux-cored arc welding. J Manuf Process 156:745-765. https://doi.org/10.1016/j.jmapro.2025.11.016

[23] Yang J, Xu S, Jia C, Han Y, Maksymov S, Wu C (2023) A novel 3D numerical model coupling droplet transfer and arc behaviors for underwater FCAW. Int J Therm Sci 184:107906. https://doi.org/10.1016/j.ijthermalsci.2022.107906

[24] Yang J, Xu S, Jia C, Han Y, Maksymov S, Wu C (2023) Numerical analysis of arc parameters and droplet behaviors for underwater flux-cored arc welding. Int J Therm Sci 194:108601. https://doi.org/10.1016/j.ijthermalsci.2023.108601

Supplementary Files

This is a list of supplementary files associated with this preprint. Click to download.

- SupplementaryMovie1.mp4
- SupplementaryMovie2.mp4
- SupplementaryMovie3.mp4
- SupplementaryMovie4.mp4